Boosting the piezoelectric coefficients of flexible dynamic strain sensors made of chemically-deposited ZnO nanowires using compensatory Sb doping

José Villafuerte, Xiaoting Zhang, Eirini Sarigiannidou, Fabrice Donatini, Odette Chaix-Pluchery, Laetitia Rapenne, Minh-Quyen Le, Lionel Petit, Julien Pernot, Vincent Consonni

Boosting the Piezoelectric Coefficients of Flexible Dynamic Strain Sensors Made of Chemically-Deposited ZnO Nanowires Using Compensatory Sb Doping

José Villafuerte,[1,2] Xiaoting Zhang,[3] Eirini Sarigiannidou,[1] Fabrice Donatini,[2] Odette Chaix-Pluchery,[1] Laetitia Rapenne,[1] Minh-Quyen Le,[3] Lionel Petit,[3] Julien Pernot,[2] and Vincent Consonni.[1*]

[1] Université Grenoble Alpes, CNRS, Grenoble INP, LMGP, F-38000 Grenoble, France

[2] Université Grenoble Alpes, CNRS, Grenoble INP, Institut NEEL, F-38000 Grenoble, France

[3] Université Lyon, INSA-Lyon, LGEF, EA682, F-69621 Villeurbanne, France

*Corresponding Author: vincent.consonni@grenoble-inp.fr

The piezoelectric devices made of ZnO nanowires have received a great interest in the past decade as potential nanogenerators and sensors. However, their characteristics are still limited significantly by the screening of the piezoelectric potential generated under mechanical solicitations, originating from the high density of free electrons in ZnO nanowires. In order to tackle that issue, we develop the compensatory Sb doping of ZnO nanowires grown by chemical bath deposition, both in the low- and high-pH regions using Sb glycolate and ammonia as chemical additives. The adsorption process of Sb(III) species on the positively charged surfaces of ZnO nanowires proceeds through attractive electrostatic forces, resulting in the significant incorporation of Sb dopants with an atomic ratio in the range of 0.11–0.45%. The optical properties of Sb-doped ZnO nanowires exhibit additional phonon modes related to Sb dopants in the range of 500–750 cm^{-1} in the Raman spectra, and some specific characteristics in the nature and intensity of radiative recombination in the cathodoluminescence spectra. Importantly, the integration of Sb-doped ZnO nanowires encapsulated in PMMA and grown on PDMS into flexible piezoelectric dynamic strain sensors is shown to drastically boost the piezoelectric charge and voltage coefficients by a factor of 2.65 and 1.91, following the significant incorporation of Sb dopants. A subsequent thermal annealing under oxygen atmosphere is revealed to further increase the piezoelectric charge and voltage coefficients by an additional factor of 1.38 and

1.49, following the activation of Sb doping and engineering of hydrogen-related defects. Two figures-of-merit are eventually derived from the piezoelectric charge and voltage coefficients and their values for flexible piezoelectric composites made of annealed Sb-doped ZnO nanowires are compared to more conventional piezoelectric materials, showing their high potential for medical devices. The present findings highlight the strategy consisting in simultaneously introducing compensatory acceptors and engineering hydrogen-related defects to reduce the screening effect, representing an additional powerful tool to enhance the characteristics of the piezoelectric devices integrating ZnO nanowires.

KEYWORDS

ZnO nanowires, chemical bath deposition, Sb doping, flexibility, dynamic strain sensors, piezoelectric coefficients

1. Introduction

The growth of ZnO nanowires (NWs) *via* the low-temperature and low-cost method of chemical bath deposition (CBD) has gained great attraction due to the existing opportunity to develop devices for the fields of chemical and/or biological sensing,[1-4] photovoltaics,[5] optoelectronics,[6-8] piezotronics,[9] and piezoelectricity.[10, 11] Among them, the piezoelectric devices made of ZnO NWs in the vertically integrated configuration are of high interest for converting biomechanical energy,[12] mechanical energy,[13] vibrational energy,[14] and hydraulic energy[15] into electrical energy for power supply and strain/stress sensing. They are supposed to exhibit several assets including larger piezoelectric coefficients at nanoscale dimensions, resistance to extremely large elastic strain without fracture, higher force-to-displacement sensitivity, high speed and lightness.[16] However, they face so far a critical challenge limiting the output voltage, namely the high density of free electrons in ZnO NWs resulting in the significant screening of the piezoelectric potential generated under mechanical solicitations.[17] Their high aspect ratio and the related large surface area are liable to induce their partial depletion from free electrons,[18] but these surface effects are commonly not sufficient. Along the CBD technique compatible with green chemistry[19] and flexibility,[20] ZnO NWs crystallize in a hydrogen-rich environment with other types of residual impurities coming from the chemical precursors in the surrounding aqueous media.[21-27] The nucleation of ZnO NWs is thus accompanied by the spontaneous formation of specific hydrogen- (H), nitrogen- (N), and carbon- (C) related defects on their surfaces and in their bulk.[28] In recent years, a great effort has been addressed to properly understand the influence of these intrinsic/extrinsic point defects and defect complexes governing the electronic structure properties of ZnO NWs. Starting two decades ago, Van de Walle revealed by density functional theory (DFT) calculations that interstitial H (H_i) acts as a shallow donor over the whole range of the Fermi level.[29] Consequently, the H-related defects were identified as H_i in the bond-centered site (H_{BC}),[29] and substitutional hydrogen on the oxygen lattice site (H_O), both of them acting as shallow donors.[30] More recently, zinc vacancy-hydrogen (V_{Zn}-nH) complexes were also investigated, where n represents the number of H_i atoms,[31, 32] and the V_{Zn}-1H, V_{Zn}-2H, and V_{Zn}-3H complexes were found to act as a deep acceptor, neutral defect, and shallow donor, respectively.[33] Due to the verified presence of H_{BC}, H_O and V_{Zn}-3H acting as shallow donors, a high density of free electrons in the range of 2.7×10^{18} to 3.1×10^{19} cm^{-3} in spontaneously grown ZnO NWs by CBD and 6.4×10^{17} to 1.1×10^{19} cm^{-3} in selective area grown ZnO nanorods by CBD was determined using four-point probe resistivity measurements.[33, 34] Hence,

these H-related defects are the major source of *n*-type conductivity in unintentionally doped ZnO NWs grown by CBD.[33, 34] Regarding the N-related defects, a recent study showed by DFT calculations and Raman scattering that the V_{Zn}-N_O-H defect complex acts as a deep acceptor and it possesses an interesting activation mechanism by thermal annealing at ~500 °C *via* the combination of N_O-H defects with V_{Zn}.[35] To reduce the density of free electrons in ZnO NWs grown by CBD strengthening the screening of the piezoelectric potential,[36-39] a special attention has recently been brought to engineer the intrinsic/extrinsic point defects and defect complexes in unintentionally doped ZnO NWs. This has included (i) the initial adjustment of the pH of the CBD solution to modify the oxygen chemical potential (μ_O) and consequently the formation energy of point defects,[40] (ii) the post-deposition thermal annealing under oxygen atmosphere,[35] and (iii) the post-deposition plasma treatments.[41] Although these strategies have been shown to significantly affect the nature and amount of H- and N-related defects in ZnO NWs, they are still not sufficient to significantly boost the characteristics of piezoelectric devices.

An alternative, additional strategy to be considered toward the fabrication of ZnO NWs with a lower density of free electrons consists in incorporating *p*-type dopants to act as compensatory acceptors.[42] Different *p*-type doping methodologies for N,[43] copper,[44] and antimony (Sb)[45, 46] have specifically been developed when using the CBD and hydrothermal growth techniques. Among them, Sb-doped ZnO NWs have elegantly been manufactured by Wang *et al*. using Sb glycolate (SbG_2^-),[46] and hence Sb may be a promising dopant to deliver stable *p*-type conductivity with efficient piezoelectric properties in sensing and energy conversion applications.[46-48] Furthermore, it was suggested that the incorporation of Sb atoms in the wurtzite structure of ZnO could form Sb_{Zn}-$2V_{Zn}$ defect complexes exhibiting a low formation energy and a small ionization energy.[49] More recently, it was also reported that the Sb_{Zn}-$3V_{Zn}$ defect complex may constitute a more stable configuration and act as a deep acceptor.[50] Along with theoretical studies on the formation energy of these defects, Sb atoms were found to substitute for the Zn lattice sites in ZnO *via* the analysis of β-particle emission at CERN's online isotope separator facility ISOLDE.[51] However, the incorporation process of Sb dopants into ZnO NWs grown by CBD is still open and the physicochemical processes in the chemical bath have not been elucidated yet, while the effect on the H- and N-related defects for the compensatory process along with the impact on the characteristics of related piezoelectric devices have not been assessed.

In the field of piezoelectric applications, ZnO NWs might act as building blocks in biosensors for the cardiac surgery of mitral valve.[52] Currently, the success of mitral valve repair is assessed *via* echocardiography, providing

precise real-time morphological analyses and functional parameters based on heuristic approximations. Unfortunately, such a technique was revealed to be insufficient to predict mid-term postoperative failure at the time of the repair.[53] Consequently, the development of piezoelectric dynamic strain sensors to measure new physical parameters, in addition to echocardiography, could allow physicians to significantly improve their abilities to perform effective and long-lasting repairs at a greater frequency.[54] The first prototype was built using piezoresistive materials, with the aim of demonstrating the possibility of measuring the force of coaptation of mitral valve, which is considered as a key parameter to help the understanding of mitral valve pathology.[55] The piezoresistive materials have been revealed to be easily processed, cost-effective, miniaturizable, and adaptable to printing technology,[56, 57] which make them as one of the most widely used in sensing devices, mainly as strain gage. However, contrarily to the piezoelectric materials, the strain gage is passive and thus needs a conditioning circuit to convert a resistance variation to an output voltage. The output voltage is thus relatively sensitive to noise owing to the poor signal-to-noise ratio. Accordingly, the signal induced from the strain gage is usually filtered to remove high-frequency noises, resulting in signal distortion due to harmonics alteration. Other limitations of the piezoresistive materials are related to drift effect (meaning derived signal in a long-time measure), and nonlinear response especially when being subjected to a bending excitation driven by the mitral valve.[55] Piezoelectric materials have nevertheless been demonstrated to be efficient not only in compression mode,[58, 59] but also in bending mode.[60, 61] Moreover, these materials deliver an output voltage merely in the case of dynamic mechanical solicitations, which in turn results in no drift effect. Such exceptional features undoubtedly make piezoelectric dynamic strain sensors as promising candidates for the characterization of mitral valve, which could overcome the technological lock of the first sensor network prototype.

In this study, we prepare Sb-doped ZnO NWs by CBD with $[SbG_2^-]$ / $[Zn(NO_3)_2]$ ratios of 0.0, 0.2, 1.0 %. To elucidate the physicochemical processes at work in the chemical bath *via* the influence of pH, the NWs are grown in the distinctive low- and high-pH regions with an initial pH (pH_0) of ~6.6 and ~10.8, respectively. The morphological properties are investigated by field-emission scanning electron microscopy (FESEM) and X-ray diffraction (XRD) measurements. The incorporation process of Sb dopants is evaluated with a combined analysis of thermodynamic computations of the nature/concentration of Zn(II) and Sb(III) species, along with the *in situ* measurements of pH and temperature during the growth. Elemental maps performed with FESEM and scanning transmission electron microscopy (STEM) using energy-dispersive X-ray spectroscopy (EDS), temperature-

dependent Raman spectroscopy and 5 K cathodoluminescence spectroscopy measurements give further evidence of the incorporation process of Sb dopants and of H- and N-related defects into ZnO NWs as well as of their activation using one-step and two-step thermal annealing conditions under oxygen atmosphere. ZnO NWs on PDMS substrates are eventually integrated into flexible piezoelectric devices within a vertically integrated configuration (*i.e.* 1-3 connectivity pattern) as dynamic strain sensors. A drastic improvement of the characteristics of piezoelectric dynamic strain sensors integrating ZnO NWs grown by CBD and following the thermal annealing and Sb-doping strategies is shown through the determination of the piezoelectric charge (d_{33}) and voltage (g_{33}) coefficients.

2. Experimental and theoretical sections

2.1. Synthesis and Thermal Annealing of ZnO nanowires

Substrates of silicon (100) and Corning glass 1737 were cleaned with ultrasonic bath in acetone and isopropyl alcohol to remove surface organic contaminants and residual dust particles. The substrates were mechanically dipped into a ZnO sol-gel solution and subsequently annealed following the methodology detailed in refs.[33, 62], to form a ZnO seed layer. As proposed by Wang *et al*., the Sb-dopant solution consisting of antimony glycolate (SbG_2^-), was prepared *via* the dissolution of antimony (III) acetate ($(CH_3CO_2)_3Sb$, Sigma-Aldrich) in a sodium glycolate solution at a 1:12 ratio.[46] ZnO NWs were grown by CBD in a sealed reactor at 85 °C containing deionized water-based solutions of zinc nitrate hexahydrate ($Zn(NO_3)_2{\cdot}6H_2O$, Sigma-Aldrich) and hexamethylenetetramine (HMTA) ($C_6H_{12}N_4$, Sigma-Aldrich) mixed in an equimolar ratio of 30 mM.

As detailed on **Table 1**, the initial pH of the solution (pH_0), with the respective $[SbG_2^-]$ / $[Zn(NO_3)_2]$ ratio for each sample, were prepared by the addition of ammonia (NH_3, Sigma-Aldrich) and the Sb-dopant solution, SbG_2^-, respectively. Finally, two different conditions of thermal annealing under oxygen atmosphere were performed: (a) one-step annealing at 300 °C for 4 h, and (b) two-step annealing at 300 °C for 4 h plus a consecutive 1 h at 450 °C.

Table 1. CBD conditions for the series of ZnO NWs grown with the respective $[SbG_2^-]$ / $[Zn(NO_3)_2]$ ratio and pH_0.

pH region	$[SbG_2^-]$ / $[Zn(NO_3)_2]$	$[NH_3]$ added (mM)	pH_0
Low-pH region	0.0 %	0	6.42
	0.2 %	0	6.66
	1.0 %	0	6.65
High-pH region	0.0 %	690	10.84
	0.2 %	694	10.78
	1.0 %	707	10.83

A 0.5 mm-thick elastic silicone elastomer sheet (PDMS, Goodfellow) was employed as a flexible substrate to fabricate the piezoelectric sensor. A 40 nm-thick ZnO seed layer was deposited on top of a clean PDMS substrate *via* dip-coating procedure. Subsequently, the whole structure was immersed in an equimolar proportion of the CBD precursors, as previously detailed. After that, a 2 µm-thick poly(methyl methacrylate) (PMMA) thin film was spin coated as an interstitial insulating matrix between the ZnO NWs and as a top insulating layer. The $[SbG_2^-]$ / $[Zn(NO_3)_2]$ ratio and thermal annealing conditions used for the ZnO NWs based piezoelectric dynamic strain sensors are detailed in **Table 2**. Finally, thin gold electrodes of 25 nm thickness and 10 mm diameter were coated on both sides of NWs composite films, using a sputter coater (Cressington, 208HR).

Table 2. CBD conditions for the series of ZnO NWs based piezoelectric devices.

Sample	Thermal annealing	$[SbG_2^-]$ / $[Zn(NO_3)_2]$
PDMS/as-grown ZnO NWs	Not annealed	0.0 %
PDMS/annealed ZnO NWs	220 °C (O_2 atm, 2 hours)	0.0 %
PDMS/as-grown Sb-doped ZnO NWs	Not annealed	1.0 %
PDMS/annealed Sb-doped ZnO NWs	220 °C (O_2 atm, 2 hours)	1.0 %

2.2. Characterization Techniques

During the ZnO NWs growth, the *in situ* measurement of pH and temperature was performed with an InLab Versatile Pro pH electrode from Mettler Toledo. The morphology of ZnO NWs was evaluated with a FEI Quanta 250 FESEM instrument. FESEM-EDS spectra were recorded on single ZnO NWs using a Bruker X-ray detector incorporated in the FEI Quanta 250 FESEM operating at 15 kV. XRD patterns were collected with a Bruker D8 Advance diffractometer using Cu Kα1 radiation (λ = 0.15406 nm) according to the Bragg-Brentano configuration, with an instrumental shift corrected by aligning the Si(400) diffraction peak to its theoretical value of 69.132°. The ZnO diffraction peaks were indexed according to the ICDD 00-036-1451 file. STEM specimens were prepared by dispersing ZnO NWs on a copper grid, using a diamond tip. STEM-EDS spectra and maps of single/dispersed ZnO NWs were collected with a JEOL SDD Centurio detector having a solid angle of up to 0.98 steradians incorporated in the JEOL 2100F field-emission-gun scanning electron microscope operating at 200 kV and having a 0.2 nm resolution in the scanning mode. The nature of the Sb-, N- and H-related defects was investigated by Raman and 5 K cathodoluminescence spectroscopy. The Raman spectroscopy of ZnO NWs was performed with a Horiba/Jobin Yvon Labram spectrometer equipped with a liquid nitrogen-cooled CCD detector. A 514.5 nm Ar^+ laser was focused on the sample surface to a spot size ~1 µm^2 with ~0.44 mW power using a 100× objective. The integration time was

of 200 s per spectral window from 50 cm^{-1} to 3750 cm^{-1}. A silicon reference sample was used for spectrum calibration at room temperature, with the theoretical Raman line set to 520.7 cm^{-1}. Additionally, an *in situ* postdeposition annealing was performed under an O_2 atmosphere from room temperature to 500 °C, using a 50× objective. The temperature control was performed using a commercial Linkam heating stage (THMS600). The Raman analysis was achieved in a $z(-,-)\bar{z}$ geometry, probing the array of ZnO NWs from the top. The 5 K cathodoluminescence acquisition was performed on top of an array of vertically aligned ZnO NWs with a FEI Inspect F50 FESEM instrument equipped with Gatan CF302 a liquid helium-cooled stage. An electron beam with low acceleration voltage of 5 kV and a small spot size (i.e., less than 10 nm) were used to probe the array of ZnO NWs in fast scan mode over an area of 2.5 x 2.5 μm^2. A parabolic mirror controlled with nanomanipulators helped to collect the cathodoluminescence signal on a 550 mm focal length monochromator (Horiba iHR550) equipped with 600 grooves/mm diffraction grating. Cathodoluminescence spectra were recorded with a thermoelectric cooled silicon CCD detector (Andor Technology Newton CCD DU940-P-BU).

The flexible ZnO NW composites were clamped in a sample holder (AMETEK, 12962a) to measure their dielectric spectra with the help of a spectrum analyzer (Solartron, 1255) and a dielectric interface (Solartron, 1296A). The measurements were performed with a driven alternating voltage (V_{RMS} = 200 mV) in a large frequency range of 0.1 Hz to 1 MHz. The piezoelectric characterizations were carried out in a specific test bench that has been described in refs. [63, 64]. In short, the samples were mechanically excited with a sinusoidal signal at 1 Hz and increasing amplitudes of force (F), meanwhile the generated charges (Q) were synchronously collected and measured in a high-sensitivity charge meter (KISTLER, Type 5015) through a short-circuit loop. The piezoelectric charge coefficient (d_{33}) was estimated as follows:

$$d_{33} = \frac{Q}{A_{active}} * \frac{A}{F} \qquad (1)$$

where A_{active} and A denote the surface areas of the gold electrode and the clamped surface, respectively. The d_{33} piezoelectric charge coefficient in turn led to an estimation of the piezoelectric voltage coefficient (g_{33}) based on the measurement of the dielectric constant (ε_r). To a practical point-of-view, measuring the charge (or current) generated by a high-impedance piezoelectric material in a short circuit condition where external perturbations are minimized is much easier to determine the g_{33} value. Inversely, measuring the voltage in an open circuit condition

to determine the g_{33} value is not applicable in a low-frequency domain because of the electrical impedance mismatch of the circuit.

2.3. Thermodynamic Computations

Thermodynamic simulations were performed with the Visual MINTEQ software to determine the speciation diagrams of Zn(II) and Sb(III) species as well as the theoretical solubility plots of ZnO at 25 °C and 85 °C at each NH_3 concentration. For the present conditions, the Zn^{2+} cation in aqueous solution is capable of forming hydroxide, amine, glycolate and/or acetate complexes with the possible ligands (HO^-, NH_3, G^- and CH_3COO^-) denoted as L. The Sb^{3+} cation in aqueous solution is capable of complexing with hydroxide and glycolate ligands. Given the general reactions $nM^{x+} + iL \leftrightarrow M_nL_i^{\,n.x+}$, where $M_nL_i^{\,n.x+}$ is the complex considered with i as the coordination number. The related stability constants β_i^L associated with each reaction are given by $\beta_i^L = \frac{[M_nL_i^{n\cdot x+}]}{[M^{x+}]^n[L]^i}$. These constants at room temperature were taken from the National Institute of Standards and Technology (NIST) database and the constants at 85 °C were deduced from Van't Hoff relation. To calculate the theoretical solubility plots for each condition, Zn- and Sb-related oxides and hydroxides were considered.

3. Results and discussion

3.1. Effect of Sb-Doping on the Growth Mechanism of ZnO Nanowires

Description of the Structural Morphology of ZnO Nanowires

The heterogeneous formation of vertically aligned, unintentionally doped and Sb-doped ZnO NWs was performed on polycrystalline ZnO seed layers oriented along the polar *c*-axis. The grains with semipolar and polar orientations act as preferential sites for the homo-epitaxial nucleation of ZnO NWs.[62, 65, 66] The morphological properties of ZnO NWs as-grown by CBD with $[SbG_2^-]$ / $[Zn(NO_3)_2]$ ratios of 0.0%, 0.2%, and 1.0% in the low-pH and high-pH regions are shown in **Figure 1a** using FESEM imaging. The resulting axial growth rate, radial growth rate, aspect ratio, and apparent density of ZnO NWs as defined in ref. [40] are presented for each CBD condition in **Figure 1b**.

The unintentionally-doped ZnO NWs as-grown by CBD in standard conditions used in the low-pH region present the characteristic wide-hexagonal shape of their wurtzite structure,[40, 67] as well as the typical axial and radial growth rates of about 298 and 26 nm/h, respectively.[33, 40] Their aspect ratio is accordingly of about 11. The morphology of Sb-doped ZnO NWs grown with $[SbG_2^-]$ / $[Zn(NO_3)_2]$ ratios of 0.2 % and 1.0 % in the low-pH region

shows no change in their wide-hexagonal shape when nucleated under the presence of SbG_2^- ions. The moderate decrease in the apparent density and slight increase in the aspect ratio may suggest a preferential interaction of the SbG_2^- ions with the polar *c*-plane. Furthermore, a slight change in the axial and radial growth rates occurs following the introduction of SbG_2^- species in the chemical bath. The undoped ZnO NWs as-grown by CBD in the high-pH region present a tapered hexagonal tip with a drastic increase in the axial and radial growth rates up to about 2053 and 36 nm/h, respectively. Their aspect ratio is consequently of about 57. Further increasing the $[SbG_2^-]$ / $[Zn(NO_3)_2]$ ratios from 0.0 % to 1.0 % along the high-pH region results in a significant increase in the axial growth rate of Sb-doped ZnO NWs up to 2524 nm/h and a much more pronounced increase in their radial growth rate up to 64 nm/h. The aspect ratio accordingly decreases down to a value of about 40, which may indicate a preferential interaction of the SbG_2^- ions with the non-polar *m*-planes. Additionally, the increase in the radial growth rate accounts for the coalescence of Sb-doped ZnO NWs grown with $[SbG_2^-]$ / $[Zn(NO_3)_2]$ ratios of 0.2 % and 1.0 % in the high-pH region and the resulting formation of a columnar film structure at their bottom. Overall, the present investigation is in agreement with Li *et al*. showing that the increase of the amount of Sb-dopants promotes the formation of tapered ZnO nanocones with faceted terraces due to an increase in the radial growth and the modified kinetics from the adsorption of SbO_X species.[68]

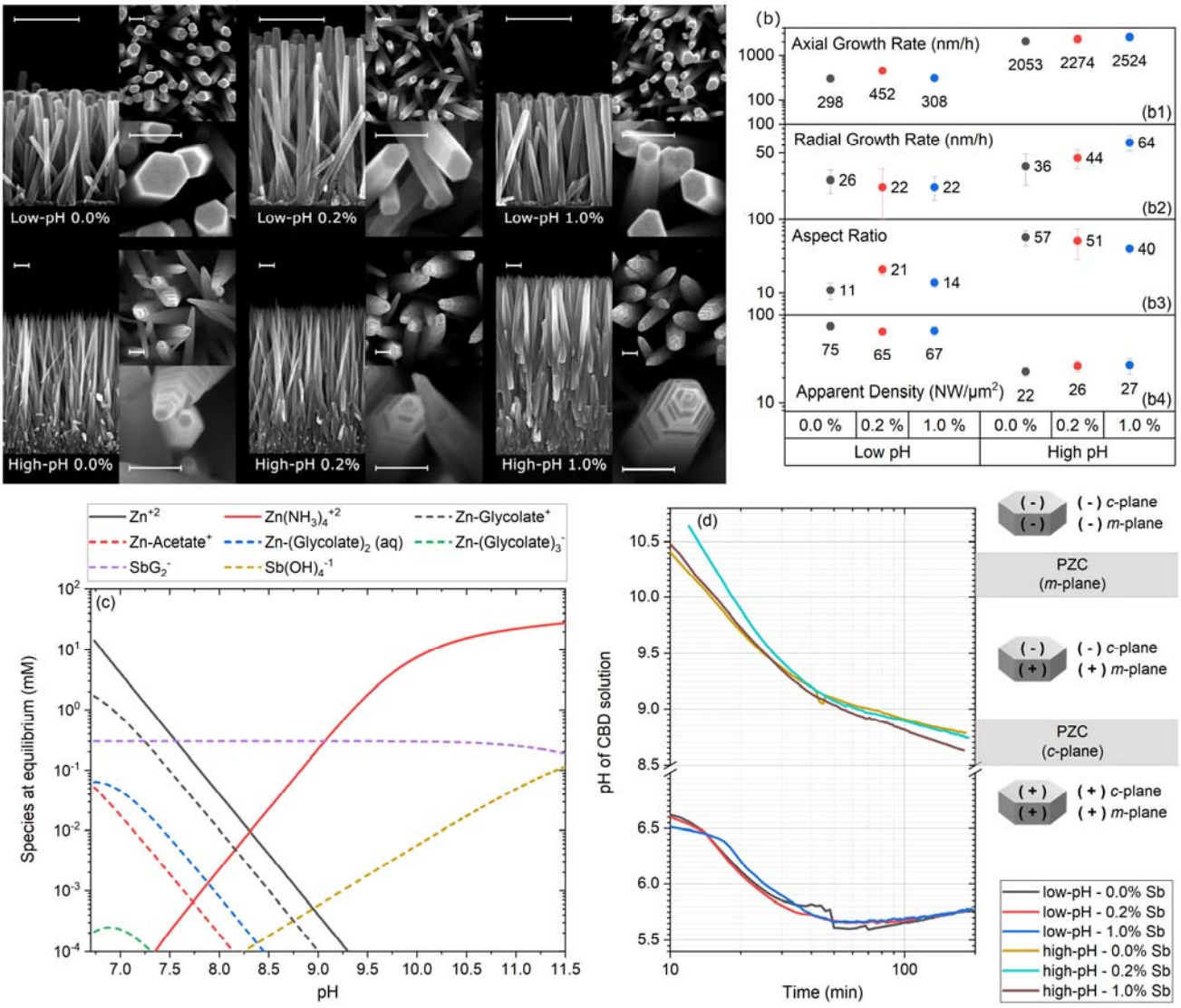

Figure 1. Cross-sectional- and top-view FESEM images of ZnO NWs as-grown by CBD with $[SbG_2^-]$ / $[Zn(NO_3)_2]$ ratios of 0.0 %, 0.2 %, and 1.0 % in the low-pH (first row) and high-pH regions (second row). The scale bars for the cross-sectional view and top-view images are 500 nm and 100 nm, respectively. Evolution of the (b1) axial growth rate, (b2) radial growth rate, (b3) aspect ratio, and (b4) apparent density of ZnO NWs grown by CBD as a function of the $[SbG_2^-]$ / $[Zn(NO_3)_2]$ ratio in the low-pH and high-pH regions. (c) Speciation diagram of the main Zn(II) species and Sb(III) species present in the chemical bath at 25 °C as a function of pH with a $[SbG_2^-]$ / $[Zn(NO_3)_2]$ ratio of 1.0 %, as computed with Visual MINTEQ software. The initial concentration of Zn^{2+} and Sb^{3+} ions corresponds to 30 mM and 0.3 mM, respectively. The solid lines represent the Zn(II) species expected to form in a standard CBD growth,[35] while the dashed lines represent the additional Zn(II) and Sb(III) species formed owing to the incorporation of SbG_2^- species in the chemical bath. (d) *In situ* measurements of the pH during the CBD of ZnO NWs using pH_0 values in the range of 7.00 – 11.07. The solid lines represent the pH of the chemical bath at a given growth time. The schematic diagrams show the surface electrical charge of the different crystallographic planes of ZnO NWs according to the expected PZC values as reported in refs.[26, 69-71].

Physicochemical and adsorption processes related to Sb(III) species and its dependence on the pH

The spontaneous growth of unintentionally-doped ZnO NWs by CBD has mostly been studied using standard conditions with $Zn(NO_3)_2$ and HMTA in the low-pH region, namely without the addition of ammonia.[23, 24, 33, 35] Following the addition of ammonia, the influence of the pH of the chemical bath has been studied for unintentional doping[24, 40] and intentional doping of ZnO NWs with Al, Ga, and Cu through successive adsorption and incorporation processes.[44, 72-74] Aiming at the intentional doping with Sb, the influence of the pH of the chemical bath and of the amount of Sb(III) species is assessed by thermodynamic computations using Visual MINTEQ software. A $[SbG_2^-]$ / $[Zn(NO_3)_2]$ ratio of 1.0 % was used for the thermodynamic computations along with an initial concentration of Zn^{2+} and Sb^{3+} ions set to 30.0 mM and 0.3 mM, respectively, and the concentration of NH_4^+ varying up to 1600 mM. A speciation diagram of Zn(II) and Sb(III) species at 25 °C is presented in **Figure 1c** and shows the nature of the pH-dependent species at equilibrium. As discussed in ref.[40], Zn^{2+} ions and $Zn(NH_3)_4^{+2}$ ion complexes are the main Zn(II) species in the low-pH and high-pH regions, respectively. The incorporation of the Sb(III) species promotes the formation of additional Zn(II)-acetate and Zn(II)-glycolate complexes, which are expected to have a negligible effect on the CBD of ZnO NWs.[46] The Sb^{3+} ions are prevented from hydrolyzing in neutral un-dissociated $Sb(OH)_3$ species *via* the complexation process with α-hydroxycarboxylate ions.[46, 75] Hence, the Sb(III) species present in the chemical bath are primarily SbG_2^- complexes with a concentration of ~0.3 mM along the wide pH range of 6.5 to 11.0. Interestingly, $Sb(OH)_4^-$ complexes start to get more significant at a pH value higher than 11.0, for which ZnO NWs do not form anymore owing to the high solubility of ZnO at this high pH.[40, 74] To further understand the growth of ZnO NWs and complement the thermodynamic computations, *in situ* pH measurements of the chemical bath are shown in **Figure 1d**. A duration of around 20 min is required for the sealed reactor to reach a temperature of ~65 °C and promote the elongation of ZnO NWs.[24] As discussed in refs. [26, 40, 46, 68, 76], specific physicochemical processes and thermodynamic considerations related to surface energy minimization, kinetically-controlled diffusive mechanisms and electrostatic forces are needed to fully understand the behavior of SbG_2^- complexes along the nucleation and elongation processes of ZnO NWs. The selected pH_0 values for the low-pH region (~6.6) and high-pH region (~10.8) lead to the nucleation and elongation of ZnO NWs by CBD under intermediate supersaturation conditions, where the metastable domain with both heterogeneous and homogeneous growths occur.[27, 77] These deposition mechanisms in the low-pH and high-pH regions have been shown to follow the mechanisms discussed by D.

Lincot.[27, 40] The right section of **Figure 1d** depicts the sign of the pH-dependent surface electrical charge of ZnO NWs according to the point-of-zero-charge (PZC) values.[26, 69-71] The growth in the low-pH region occurs when both the polar *c*- and non-polar *m*-planes are positively charged. In contrast, the growth in the high-pH region occurs when the pH curves cross the PZC of the non-polar *m*-planes, leaving the *m*-plane positively charged and the *c*-plane negatively charged. These conditions require the consideration of two specific pH-dependent processes for the adsorption of Sb(III) species on the surfaces of ZnO NWs: (i) the electrostatic interactions between the negatively charged SbG_2^- complexes and the positively/negatively charged planes, and (ii) the magnitude of the zeta potential. The zeta potential, also known as the electrokinetic potential, defines the potential difference between the external surfaces of the ZnO NW and the surrounding liquid.[69, 78] In **Figure 1d**, the magnitude of the zeta potential increases as the pH values get farther from the PZC.[69] In the low-pH region, SbG_2^- complexes are electrostatically attracted by both the polar *c*- and non-polar *m*-planes, and the magnitude of the zeta potential is large, as reported by Degen *et al.*[69] In contrast, in the high-pH region, the magnitude of the zeta potential is considerably smaller and the adsorption process of SbG_2^- complexes exclusively proceeds on the positively charged non-polar *m*-planes, hence promoting the drastic increase in the radial growth of ZnO NWs as in the case of Ga(III) species[74] and the formation of faceted terraces as observed in **Figure 1**. Then, by comparing the low- and high-pH regions, we may elucidate that the adsorption of SbG_2^- complexes at low-pH mainly occurs through the polar *c*-plane located on the tip of ZnO NWs. This can be supported by (i) the promoted development of ZnO NWs with a moderate increase in the axial growth rate, and (ii) the slower growth rate of the non-polar *m*-planes could favor a more efficient adsorption process of SbG_2^- complexes on the polar *c*-plane, which is known to be highly reactive.[76] Additionally, the adsorption process of SbG_2^- complexes could also affect the capping process operating with HMTA molecules on the non-polar *m*-planes.[25]

3.2. Effect of Sb-Doping on the Incorporation Mechanism of Dopants into ZnO Nanowires

To reveal the presence of Sb dopants within the ZnO NWs, FESEM-EDS and XRD measurements are presented in **Figure 2**. The presence of Sb atoms was assessed by FESEM-EDS measurements in **Figure 2a,b**, where all the spectra were normalized with respect to the Zn K_β line at 9.57 keV and recorded under identical conditions. ZnO NWs grown by CBD with $[SbG_2^-]$ / $[Zn(NO_3)_2]$ ratios of 0.2 and 1.0 % exhibit the specific peaks pointed at 3.604 and 3.842 keV, which are assigned to the Sb $L\alpha_1$ and Sb $L\beta_1$ lines, respectively, both in the low-pH and high-pH

regions. In contrast, the two Sb-related peaks do not occur in unintentionally-doped ZnO NWs, regardless of the pH region. Following a semi-quantitative analysis performed on the Sb $L\alpha_1$ line in the FESEM-EDS spectra, the Sb/Zn element ratio in the low-pH (high-pH) region is equal to 0.16 and 0.45 % (0.11 and 0.21 %) for the 0.2 and 1.0 % $[SbG_2^-]$ / $[Zn(NO_3)_2]$ ratios, respectively. This reveals that a larger amount of Sb atoms has been incorporated into ZnO NWs when grown in the low-pH region as compared to those grown in the high-pH region. The higher incorporation of Sb atoms in the low-pH region strongly agrees with the enhanced adsorption process of SbG_2^- complexes on both the polar *c*- and non-polar *m*-planes of ZnO NWs, which originates from the attractive electrostatic forces. It should be noted here that increasing further the $[SbG_2^-]$ / $[Zn(NO_3)_2]$ ratio above 1 % in the low-pH region would not result in a significant increase in the Sb/Zn element ratio beyond 0.45 % in Sb-doped ZnO NWs owing to Sb solubility-related considerations.

The XRD patterns as presented in **Figure 2c,d** reveal the characteristic wurtzite structure for all the *c*-axis oriented unintentionally-doped and Sb-doped ZnO NWs through the strong intensity of the (0002) diffraction peak at 34.4°. A higher magnification around the (0004) diffraction peak is presented in **Figure 2e,f** to make a comparison with its theoretical value of 72.56°. The unintentionally-doped ZnO NWs as-grown by CBD in the low-pH region have the (0004) diffraction peak centered at 72.61° with a shift of +0.05° from the theoretical value. In contrast, when grown in the high-pH region, the (0004) diffraction peak is centered at 72.54° and exhibits a shift of –0.02°. Using the XRD data, the incorporation of Sb atoms was assessed through the calculated *c*-lattice parameter as seen in **Figure 2g,h**, which increases from 5.204 to 5.206 Å (5.208 to 5.209 Å) for the $[SbG_2^-]$ / $[Zn(NO_3)_2]$ ratio of 0 and 1 % in the low-pH (high-pH) region. In both pH regions, the *c*-lattice parameter increase with the $[SbG_2^-]$ / $[Zn(NO_3)_2]$ ratio has been attributed to the lattice expansion due to the incorporation of Sb dopants into the Zn lattice sites.[79-81] However, the unintentionally-doped ZnO NWs grown by CBD in the low- and high-pH regions are in a compressive and tensile strain state, respectively. The compressive strain state in the low-pH region elucidates a relaxed structure and the moderate formation of intrinsic and extrinsic point defects within the crystal structure. In contrast, the tensile strain state in the high-pH region correlates with the significant formation of V_{Zn}-related defects, as reported in ref.[40]. More importantly, the significant difference in Sb-doped ZnO NWs could elucidate the preferential incorporation of Sb dopants in either substitutional Zn or interstitial sites.[49, 50] Moreover, the Sb-doped ZnO NWs grown in the low-pH region exhibit a larger increase in the *c*-lattice parameter with the $[SbG_2^-]$ / $[Zn(NO_3)_2]$ ratio, which is associated with the more significant incorporation of Sb dopants as

detected by FESEM-EDS spectra. The smaller increase in the *c*-lattice parameter of Sb-doped ZnO NWs grown in the high-pH region with the $[SbG_2^-]$ / $[Zn(NO_3)_2]$ ratio suggests a challenged incorporation of Sb dopants. Remarkably, no additional diffraction peaks related to any residual phases coming from Sb oxides, Sb hydroxides and Sb oxide-hydroxides are detected in the XRD patterns.

The STEM-EDS spectrum and maps shown in **Figure 2i** give further evidence of the homogeneous incorporation of Sb atoms, which is illustrated here when ZnO NWs are grown with a $[SbG_2^-]$ / $[Zn(NO_3)_2]$ ratio of 1 % in the high-pH region. The Sb $L\alpha_1$ and Sb $L\beta_1$ lines are clearly shown in the inset of the Sb elemental map. The higher incorporation of Sb atoms as seen in ZnO NWs grown by CBD with a $[SbG_2^-]$ / $[Zn(NO_3)_2]$ ratio of 1 % in the low-pH region does not affect further the structural quality of their wurtzite structure as depicted in **Figure 2j**, where no specific extended defects are formed.

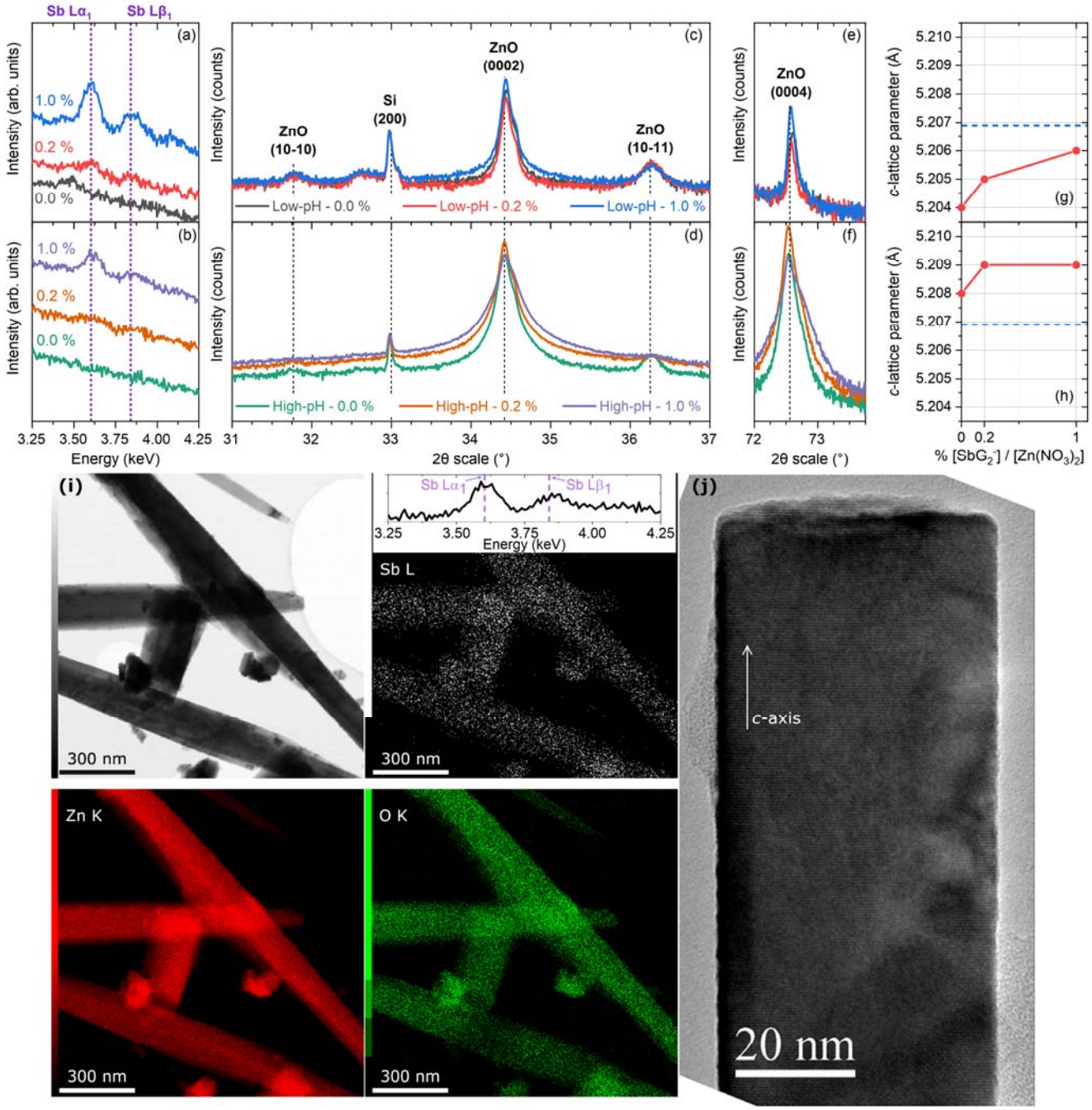

Figure 2. FESEM-EDS spectra of unintentionally-doped and Sb-doped ZnO NWs grown by CBD with $[SbG_2^-]$ / $[Zn(NO_3)_2]$ ratios of 0.0 %, 0.2 % and 1.0 % in the (a) low-pH region and (b) high-pH region. The dashed lines represent the Sb $L\alpha_1$ and Sb $L\beta_1$ theoretical lines. XRD patterns of unintentionally-doped and Sb-doped ZnO NWs grown by CBD with $[SbG_2^-]$ / $[Zn(NO_3)_2]$ ratios of 0.0 %, 0.2 % and 1.0 %, showing the characteristic (c-d) (0002) and (e-f) (0004) diffraction peaks. The dashed lines represent the theoretical position of the labeled ZnO diffraction peaks according to the ICDD 00-036-1451 file and Si diffraction peak according to ref.[82]. (g-h) Evolution of the *c*-lattice parameter as a function of the $[SbG_2^-]$ / $[Zn(NO_3)_2]$ ratio. The inset dashed line corresponds to the bulk *c*-lattice parameter as reported in ref.[83]. (i) Bright-field TEM image of dispersed Sb-doped ZnO NWs as grown by CBD in the high-pH region with a $[SbG_2^-]$ / $[Zn(NO_3)_2]$ ratio of 1.0 %, along with the respective STEM-EDS

elemental maps of the Zn (red), O (green), and Sb (white) elements. The inset shows the related STEM-EDS spectrum with an emphasis placed on the Sb $L\alpha_1$ and Sb $L\beta_1$ lines. (j) High-resolution TEM image of a single Sb-doped ZnO NW as-grown by CBD with a $[SbG_2^-]$ / $[Zn(NO_3)_2]$ ratio of 1.0 % in the low-pH region.

3.3. Raman Spectroscopy of Unintentionally-Doped and Sb-Doped ZnO Nanowires

Given the effective incorporation of Sb atoms into ZnO NWs as shown by the chemical analysis, temperature-dependent Raman scattering measurements collected in the low wavenumber range were performed to investigate in an *in situ* manner the activation of Sb dopants. They are presented in **Figure 3** in the illustrative case of ZnO NWs grown by CBD with a $[SbG_2^-]$ / $[Zn(NO_3)_2]$ ratio of 1.0 % in the high-pH region. In the low wavenumber range of 50 – 900 cm^{-1}, the Raman lines at 99 (E_2^{low}), 438 (E_2^{high}), and 574 (A_1(LO)) cm^{-1} correspond to the optical phonon modes for the wurtzite structure of ZnO NWs.[84] The Raman lines at 203 ($2TA/2E_2^{low}$) and 333 (E_2^{high}- E_2^{low}) cm^{-1} are assigned to the typical second-order modes. Interestingly, two additional modes (AMs) occur at ~525 cm^{-1} (AM_1(Sb)) and ~690 cm^{-1} (AM_2(Sb)), which are notably the two specific Sb-related vibrational modes as reported in ref.[85] in the case of Sb-doped ZnO thin films grown by pulsed-laser deposition.

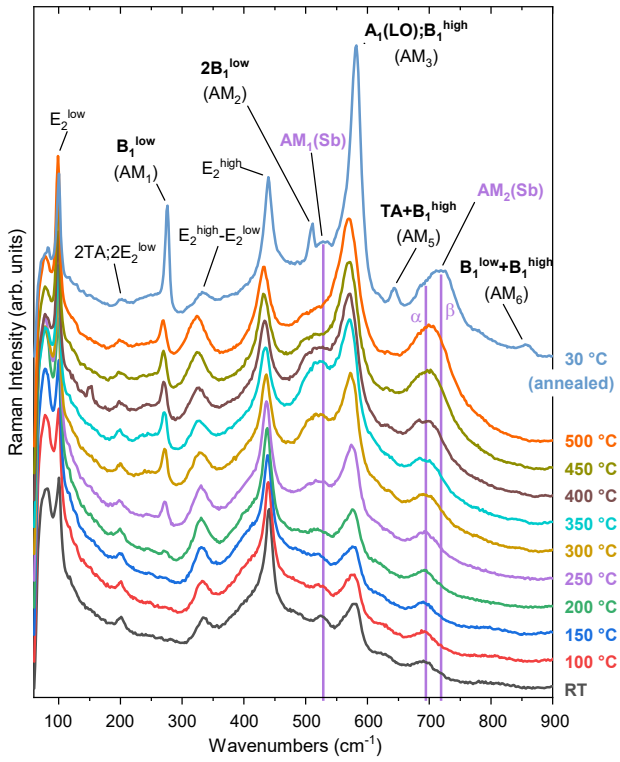

Figure 3. Raman scattering spectra of ZnO NWs grown by CBD with a $[SbG_2^-]$ / $[Zn(NO_3)_2]$ ratio of 1.0 % in the high-pH region. The spectra were collected along an *in situ* thermal annealing under oxygen atmosphere from room temperature to 500 °C and after cooling down to 30 °C. They are plotted in the low wavenumber range of 50 – 900 cm^{-1}. The inset labels show the assigned vibrational frequencies according to refs.[84-86].

While performing the *in situ* thermal annealing under oxygen atmosphere, the appearance of standard AMs in the Sb-doped ZnO NWs progressively proceeds. These standard AMs have also been reported for unintentionally doped[40] and intentionally Al- and Ga-doped ZnO NWs grown by CBD.[72-74] They are related to the presence of extrinsic impurities and attributed to dopant-induced defects in the host ZnO lattice.[85] Recently, these standard AMs have been observed in annealed ZnO NWs grown in the high-pH region and attributed to disorder-activated Raman B_1 silent modes.[40, 86, 87] Hence, the additional B_1 silent modes at 276 (AM_1 - B_1^{low}), 510 (AM_2 - $2B_1^{low}$), 581 (AM_3 - A_1(LO), B_1^{high}), 644 (AM_5 - TA+B_1^{high}), and 856 (AM_6 - B_1^{low} +B_1^{high}) cm^{-1} occur from an annealing temperature of ~200 °C. Following the thermal annealing, we can observe that the AM_1(Sb) line is still pointed at ~525 cm^{-1}, but in close proximity to the Raman lines assigned to AM_2 ($2B_1^{low}$) and AM_3 (A_1(LO), B_1^{high}). In contrast, the AM_2(Sb) line is shifted and mainly centered at ~715 cm^{-1}, while exhibiting a shoulder at its initial position of ~690 cm^{-1}. **Table 3** gives an overview of the Sb-related vibrational modes reported in the wurtzite structure of ZnO grown as thin films and NWs by different deposition techniques.[80, 85, 88-90] It is shown that the AM_2(Sb) lines have typically been reported at ~685 cm^{-1} in as-grown ZnO, but at ~712 cm^{-1} in annealed ZnO. As a result, we proceed to define the two components of the AM_2(Sb) line as AM_2(Sb)-α (~690 cm^{-1}) and AM_2(Sb)-β (~715 cm^{-1}).

Table 3. Wavenumber of the AM_2(Sb) lines measured in as-grown and annealed ZnO NWs grown by CBD with a $[SbG_2^-]$ / $[Zn(NO_3)_2]$ ratio of 1.0 % in the high-pH region. For comparison, Sb-related vibrational modes reported for different Sb-doped ZnO with the wurtzite structure are listed.

	Our data	**Literature**		
Mode	**ω_{exp} (cm^{-1})**	**ω (cm^{-1})**	**Structure, Growth method (Annealing conditions)**	**Ref.**
AM_1(Sb)	525	531	Thin film, Pulsed-laser deposition (not annealed)	[85]
AM_2(Sb)-α	690	685	Thin film, Pulsed-laser deposition (not annealed)	[85]
AM_2(Sb)-β	715	709	Film, Sol-gel (750 °C, 2 h, air)	[88]
		713	NW, Hydrothermal (950 °C, 30 min, air)	[89]
		712	Pellet, Solid State Reaction (1000 °C, 3 h, air)	[80]
		716	Nanobelt, Thermal evaporation (880 °C, 25 min, Ar/O_2)	[90]

The Raman scattering spectra collected in the low wavenumber range of unintentionally-doped and Sb-doped ZnO NWs grown by CBD with $[SbG_2^-]$ / $[Zn(NO_3)_2]$ ratios of 0.0 %, 0.2 %, and 1.0 % in the low-pH and high-pH regions are presented in **Figure 4a-f.** Three different conditions defined as the as-grown series, one-step annealing

series (300 °C for 4 h), and two-step annealing series (300 °C for 4 h as a first step, followed by 450 °C for 1 h as a second step) were investigated to reveal their effects on the Sb-doping.

The unintentionally-doped and Sb-doped ZnO NWs grown in the low-pH region as presented in **Figure 4a-c** show the characteristic optical phonon modes of the wurtzite structure as previously discussed. The as-grown and annealed unintentionally-doped ZnO NWs show the typical Raman spectra already reported in refs.[33, 35] for similar CBD and annealing conditions without any Sb-related vibrational modes. Some lines are less visible after a two-step thermal annealing due to the occurrence of a strong fluorescence process in the Raman spectra. The as-grown Sb-doped ZnO NWs present a prominent broad band from ~460 to ~560 cm^{-1}, which could be related to the incorporation of Sb atoms into ZnO NWs. The Sb-doped ZnO NWs grown with a $[SbG_2^-]$ / $[Zn(NO_3)_2]$ ratio of 0.2% show no evident AM_1(Sb) and AM_2(Sb) lines on any of the as-grown and one-step annealing conditions, but the AM_2(Sb) line slightly occurs in the two-step annealing condition. In contrast, the Sb-doped ZnO NWs grown with a $[SbG_2^-]$ / $[Zn(NO_3)_2]$ ratio of 1.0 % exhibit the AM_2(Sb) line in any of the as-grown and annealing conditions. Interestingly, the as-grown Sb-doped ZnO NWs with a $[SbG_2^-]$ / $[Zn(NO_3)_2]$ ratio of 1.0 % present the same behavior as shown in **Figure 3**, where the AM_2(Sb)-α line is centered at ~690 cm^{-1} and then it shifts to the AM_2(Sb)-β line at ~715 cm^{-1} following the one-step and two-step annealing conditions.

The unintentionally-doped and Sb-doped ZnO NWs grown in the high-pH region as presented in **Figure 4d-f** also exhibit the characteristic optical phonon modes of the wurtzite structure as previously discussed. The as-grown and annealed unintentionally doped ZnO NWs show the typical Raman spectra already reported in refs.[40] for similar CBD and annealing conditions without any Sb-related vibrational mode, as in the low-pH region. No significant fluorescence process occurs in the Raman spectra related to the two-step annealing condition. The standard AMs related to the B_1 silent modes appear after thermal annealing, as previously reported for unintentionally doped ZnO NWs grown in the high-pH region.[40] The AM_1(Sb) lines are observed in as-grown and annealed Sb-doped ZnO NWs and show a similar intensity, regardless of the $[SbG_2^-]$ / $[Zn(NO_3)_2]$ ratio. In contrast, the intensity of the AM_2(Sb) lines strongly increases as the $[SbG_2^-]$ / $[Zn(NO_3)_2]$ ratio is increased from 0.2 to 1.0 %, indicating the effective incorporation of Sb atoms into ZnO NWs. Again, the as-grown Sb-doped ZnO NWs with $[SbG_2^-]$ / $[Zn(NO_3)_2]$ ratios of 0.2 and 1.0 % present the same behavior as shown in **Figure 3**, where the AM_2(Sb)-α line is centered at ~690 cm^{-1} and then it shifts to the AM_2(Sb)-β line at ~715 cm^{-1} following the one-step and two-step annealing conditions. The existence of the two AM_2(Sb)-α and AM_2(Sb)-β lines suggests an

effective change of the neighboring electronic potential of Sb atoms within the ZnO NWs,[91, 92] promoting a change of the phonon frequencies of the crystal structure.[86, 92, 93]

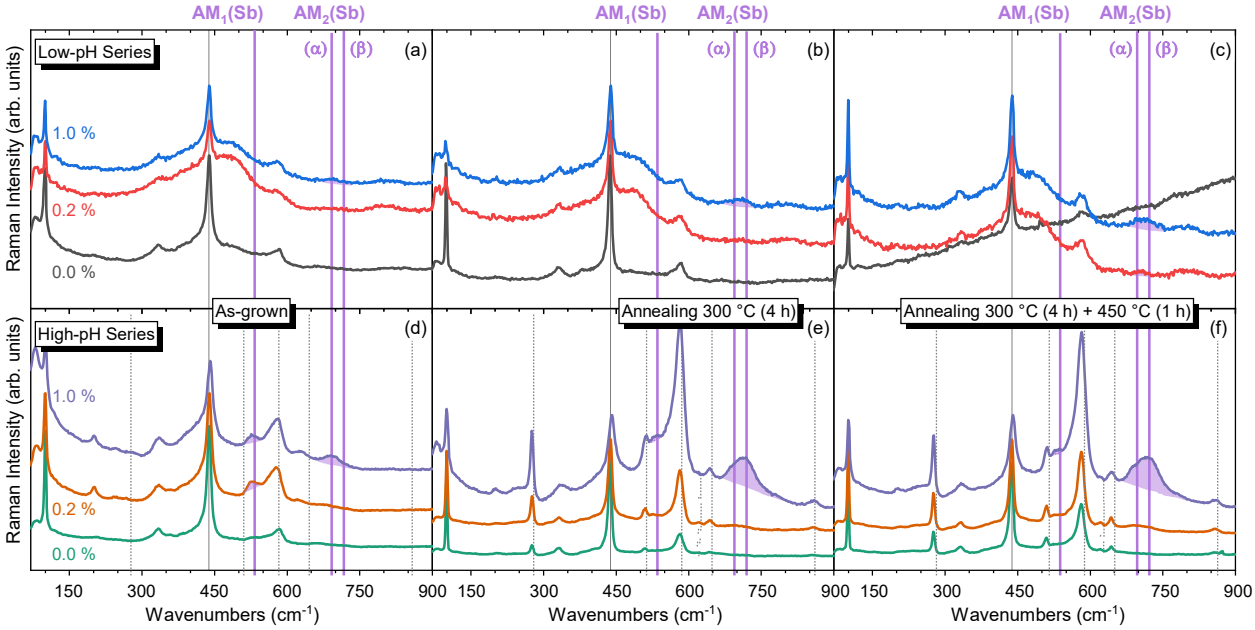

Figure 4. Raman scattering spectra plotted in the low wavenumber range of ZnO NWs grown by CBD with $[SbG_2^-]$ / $[Zn(NO_3)_2]$ ratios of 0.0 %, 0.2 % and 1.0 % in the low-pH and high-pH regions. (a,d) as-grown series, (b,e) one-step annealing series (300°C for 4 h) under oxygen atmosphere, and (c,f) two-step annealing series (300 °C for 4 h as a first step, followed by 450 °C for 1 h as a second step). The inset vertical lines represent the E_2^{high} mode (grey solid line)[84], the Sb-related vibrational modes (purple solid lines)[85], and the standard AMs related to B_1 silent modes (black dashed lines).[40, 86, 87]

The presence of C-, N-, and H-related defects is shown in the Raman scattering spectra collected in the high wavenumber range of 2600 – 3750 cm^{-1}, as presented in **Figure S1**. Within the 2850–3000 cm^{-1} range, the vibrational modes of the C–H_X groups (X = 1, 2, 3) adsorbed on the nonpolar *m*-planes and coming from residual HMTA molecules are clearly observed in unintentionally-doped ZnO NWs grown in the low-pH region.[25, 94-96] Interestingly, no relevant C–H_X modes are detected in Sb-doped ZnO NWs grown in the low-pH and high-pH regions, namely in the presence of SbG_2^- ions. This indicates a competitive adsorption process between the SbG_2^- ions and residual HMTA molecules, where the dominant adsorption of SbG_2^- ions leads to the efficient incorporation of Sb atoms and to the considerable reduction of the adsorbed C–H_X groups on the nonpolar *m*-planes. The Raman line centered at 3078 cm^{-1} is attributed to the V_{Zn}-N_O-H defect complex acting as a deep acceptor in ZnO and its presence is detected in all unintentionally-doped and Sb-doped ZnO NWs.[35, 97] Other N-related defects with a lower intensity are located at ~3121 and ~3160 cm^{-1} and are attributed to the $AB_{N\perp}$ and $AB_{N\parallel}$ configurations of the

N_O–H bonds, respectively.[35, 98] The well-defined Raman line at 3575 cm^{-1} is assigned to H_{BC} acting as a shallow donor,[99, 100] and it possesses an asymmetric shape due to vibrational modes related to O–H bonds located at 3500 cm^{-1}.[97, 99, 101] The contribution of V_{Zn}-nH (n = 1, 2, 3) defect complexes within the 3300 – 3418 cm^{-1} range is also crucial for the analysis and comparison between unintentionally-doped and Sb-doped ZnO NWs grown in the low-pH and high-pH regions.[40, 99, 102, 103] Generally, the H_{BC} line is the most prominent Raman line of the H-related defects along with the V_{Zn}-nH lines. Here, the Raman lines assigned to H_{BC} and V_{Zn}-nH defect complexes do not occur in Sb-doped ZnO NWs grown in the low-pH region, as shown in **Figure S1a**. This supports the fact that the incorporation of Sb atoms in the low-pH region affects the formation of H-related defects. In contrast, the Raman lines assigned to H_{BC} and V_{Zn}-nH defect complexes are well pronounced in Sb-doped ZnO NWs grown in the high-pH region, as revealed in **Figure S1b**. It was further reported that the intensity of the V_{Zn}-nH lines increases when growing ZnO NWs in the high-pH region, where the O-rich environment promotes the formation of V_{Zn}-related defects.[40] Sb atoms are also supposed to be incorporated into the wurtzite structure of ZnO as Sb_{Zn}-$2V_{Zn}$ [49] or Sb_{Zn}-$3V_{Zn}$ [50] defect complexes, resulting in the significant formation of V_{Zn}. Accordingly, the incorporation of Sb-related defects together with the H-rich environment accounts for the prominent increase in the intensity of the Raman lines assigned to V_{Zn}-nH defect complexes in Sb-doped ZnO NWs grown in the high-pH region with a $[SbG_2^-]$ / $[Zn(NO_3)_2]$ ratio of 1.0%. In particular, the formation of the lower coordinated V_{Zn}-H defect complexes exhibiting a Raman line at ~3420 cm^{-1} is expected following the significant formation of V_{Zn}.

3.4. Cathodoluminescence Spectroscopy of Unintentionally-Doped and Sb-doped ZnO nanowires

Given the effective incorporation of Sb dopants into ZnO NWs, its activation following thermal annealing, and its influence on the formation of H-related defects as shown by Raman spectroscopy, 5K cathodoluminescence measurements were performed to investigate the related radiative transitions in the near-band edge (NBE) and visible emission regions. The 5 K cathodoluminescence spectra of unintentionally-doped and Sb-doped ZnO NWs grown by CBD with $[SbG_2^-]$ / $[Zn(NO_3)_2]$ ratios of 0.0 %, 0.2 %, and 1.0 % in the low-pH and high-pH regions are presented in **Figure 5**, along with a zoom-in in the NBE emission region in **Figure S2**. The two different conditions defined as the one-step annealing series (300 °C for 4 h), and two-step annealing series (300 °C for 4 h as a first step, followed by 450 °C for 1 h as a second step) were again investigated to reveal their effects on the Sb-doping.

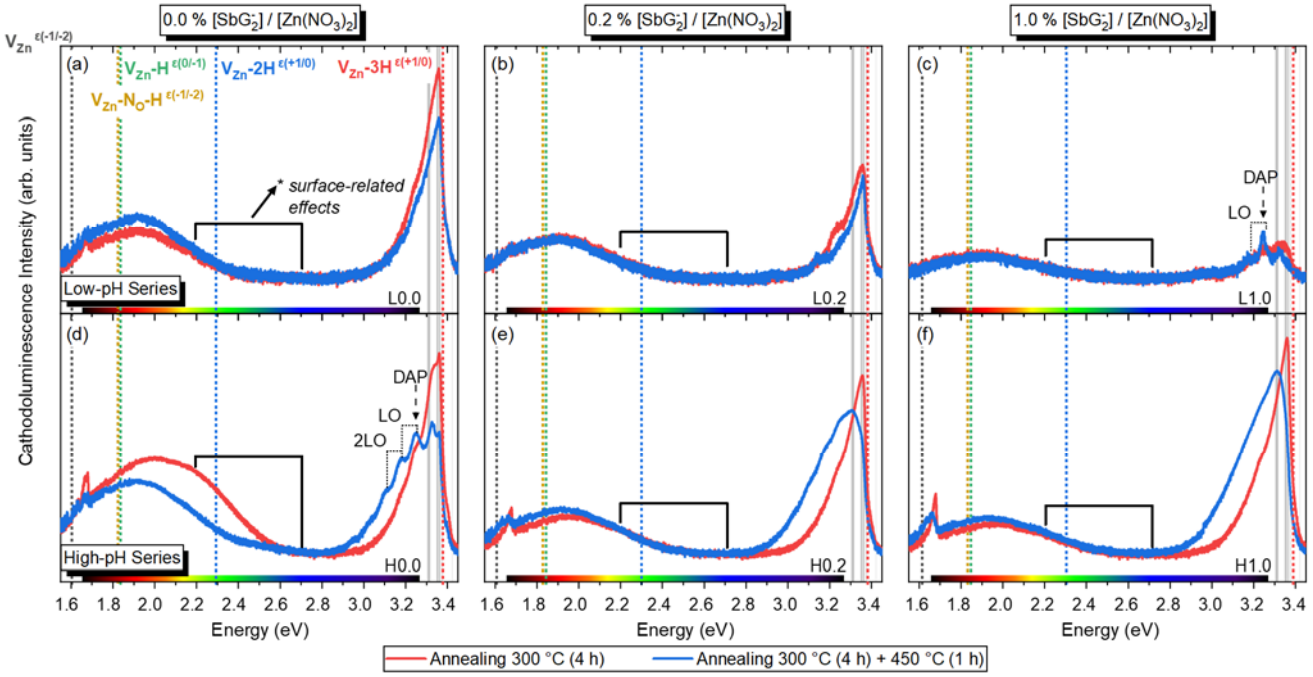

Figure 5. 5 K cathodoluminescence spectra of annealed ZnO NWs grown by CBD with $[SbG_2^-]$ / $[Zn(NO_3)_2]$ ratios of (a,d) 0.0 %, (b,e) 0.2 %, and (c,f) 1.0 % in the low-pH and high-pH regions. Two spectra are presented for each annealing condition under oxygen atmosphere: 300 °C for 4 h (red curve) and 300 °C for 4 h plus a consecutive 1 h at 450 °C (blue curve). The insets represent the emission energy of optical transitions as inferred from DFT calculations in refs.[33, 35, 102, 104].

The unintentionally doped ZnO NWs grown by CBD show a NBE emission with predominant radiative transitions involving neutral donor-bound A-excitons (D^0X_A) at 3.362 eV.[33, 35, 40] Other contributions to the NBE emission are expected from H_O (I_4), V_{Zn}-3H defect complex (I_5) and H_{BC} lines at 3.3628, 3.3614, and 3.360 eV, respectively.[33, 105-107] As shown in **Figures 5a,d** and **Figure S2a,d**, the one-step annealed unintentionally-doped ZnO NWs exhibit a strong NBE emission centered around the D^0X_A lines at ~3.359 eV and ~3.361 eV when grown in the low-pH and high-pH regions, respectively. The two-step annealed unintentionally-doped ZnO NWs exhibit a significant line centered at ~3.249 eV and attributed to donor-acceptor pair (DAP) transitions[108-110] with the respective first and second phonon replicas located at ~3.176 eV and ~3.103 eV, respectively. These DAP transitions were detected following the thermal activation of V_{Zn}-N_O-H defect complexes in ZnO NWs grown by CBD in the high-pH region and annealed at 450 °C.[40] Additionally, the D^0X_A transitions are damped and two emission lines appear at ~3.327 eV and ~3.336 eV, typically in the energy range of the two-electron satellite (TES) transitions from the I_4 lines.[106] The incorporation of Sb dopants into ZnO NWs results in a strong influence on the intensity of the NBE emission with an important difference between ZnO NWs grown in the low-pH and high-

pH regions. The NBE intensity of Sb-doped ZnO NWs grown in the low-pH region as seen in **Figures 5b,c** and **Figures S2b,c** shows an important dampening as the $[SbG_2^-]$ / $[Zn(NO_3)_2]$ ratio is increased. In contrast, the NBE intensity of Sb-doped ZnO NWs grown in the high-pH region as seen in **Figures 5e,f** and **Figures S2e,f** reveals no relevant dampening effect as the $[SbG_2^-]$ / $[Zn(NO_3)_2]$ ratio is increased. The reduction of the NBE emissions in Sb-doped ZnO NWs grown in the low-pH region could be related to the following reasons: (i) the high density of vacancies in the surface region, (ii) the competition with the radiative recombination of defects in the visible spectral region, and/or (iii) the presence of non-radiative recombination centers.[111] As presented in **Figures 5c** and **S2c**, the two-step annealed Sb-doped ZnO NWs with a $[SbG_2^-]$ / $[Zn(NO_3)_2]$ ratio of 1.0 % and grown in the low-pH region exhibit a prominent DAP emission at ~3.245 eV with a 1LO phonon replica at ~3.173 eV. This DAP emission additionally shows a high energy asymmetry which could reveal the contributions from several deep acceptors present in ZnO NWs grown by CBD, including V_{Zn}-H, V_{Zn}-N_O-H, and Sb-related defects and defect complexes.[33, 35, 49, 50] As presented in **Figure 5e,f** and **Figure S2e,f**, the two-step annealed Sb-doped ZnO NWs with $[SbG_2^-]$ / $[Zn(NO_3)_2]$ ratios of 0.2 and 1.0 % and grown in the high-pH region exhibit a dampened $D^\circ X_A$ emission and an increased red-shifted NBE emission centered at ~3.31 eV. This broad NBE is suggested to be related to neutral acceptor-bound A excitons ($A^\circ X_A$),[112] free electron-to-acceptor (FA) transitions,[113] and DAP emissions.[108-110, 114]

Along the visible spectral region, different emissions are assigned as i) the red-orange band, ii) the yellow-green band, and iii) the green-blue band, as shown in **Figure 5**. The red-orange emission band is attributed to the V_{Zn}-H $^{\varepsilon(0,-1)}$ and V_{Zn}-N_O-H $^{\varepsilon(-1,-2)}$ transition levels, both with an emission energy of 1.82 eV.[33, 35] The yellow-green emission band is attributed to the neutral V_{Zn}-2H $^{\varepsilon(+1,0)}$ transition level at 2.29 eV and to the V_{Zn}-N_O-H $^{\varepsilon(0,-1)}$ transition level at 2.27 eV.[33, 35] The green-blue emission band is attributed to N- and H-related defects including V_{Zn}-H $^{\varepsilon(+1,0)}$, V_{Zn}-H $^{\varepsilon(+2,+1)}$, V_{Zn}-2H $^{\varepsilon(+2,+1)}$, V_{Zn}-N_O-H $^{\varepsilon(+1,0)}$, V_{Zn} $^{\varepsilon(+1,0)}$, and V_{Zn} $^{\varepsilon(+2,+1)}$.[33, 35] Additionally, the green-blue emission band is labeled as surface-related effects, since it is attributed to unexpected charge states generated from the recombination of electrons with the high density of holes that migrate to the ZnO NW surfaces upon the irradiation under electron beam.[33, 115] The second order of the NBE emissions also occurs at ~1.68 eV.[116] From the different cathodoluminescence acquisitions, it is evident that the overall intensity of the defect visible band is also damped with the increase in the $[SbG_2^-]$ / $[Zn(NO_3)_2]$ ratio for both ZnO NWs grown in the low-pH and high-pH regions. The prominent phonon replica suggest a strong coupling of the A_1(LO), and/or B_1^{high} polar phonons

(~580 cm^{-1}) with the photo-generated electrons.[114] As shown in **Figure 4**, the incorporation of Sb dopants increases the phonon modes located at ~580 cm^{-1}, which act as non-radiative recombination centers. Hence, the strong dampening observed for the doped ZnO NWs grown in the low-pH region is due to the non-radiative recombination centers caused by the Sb-doping. In contrast, the moderate dampening observed for the doped ZnO NWs grown in the high-pH is due to the competitive non-radiative and radiative recombination centers (i.e. high density of Sb-related and V_{Zn}-related defects).

3.5. Effect of Sb-Doping on the Piezoelectric Properties of Flexible Devices

The incorporation of Sb dopants into ZnO NWs grown by CBD on a rigid substrate as shown by XRD, FESEM-EDS, STEM-EDS, Raman spectroscopy, and cathodoluminescence spectroscopy offers a powerful tool to improve the piezoelectric properties of nanocomposites in addition to the thermal annealing under oxygen atmosphere. In order to estimate the individual and combined effects of the Sb-doping of ZnO NWs and of the thermal annealing treatment, the fabrication of flexible devices were made of four composites as described in **Figure 6a-d**. A 0.5 mm-thick elastic silicone elastomer sheet (PDMS) was used as a flexible substrate, on top of which a 40 nm-thick polycrystalline ZnO seed layer was deposited by dip coating. The unintentionally-doped ZnO NWs grown in the low-pH region were deposited by CBD as a reference and subsequently annealed at 220 °C for 2 hours under oxygen atmosphere. The Sb-doped ZnO NWs grown with a $[SbG_2^-]$ / $[Zn(NO_3)_2]$ ratio of 1.0 % in the low-pH region, where the incorporation of Sb dopants is the most important, were also deposited by CBD and annealed under the same conditions. The unintentionally-doped and Sb-doped ZnO NWs were then encapsulated by a PMMA polymer matrix of 2 µm-thickness deposited by spin coating to ensure the mechanical stability and the electromechanical coupling. Also, it allowed to form an insulating top layer favorable for the capacitive configuration of piezoelectric devices. Two gold electrodes of 25 nm-thickness and 10 mm-diameter were eventually deposited with a sputter coater on both sides of the composites. The main objective consists here in both reducing and compensating for the high density of free electrons in ZnO NWs, which is typically measured regardless of the deposition techniques used.[117, 118]

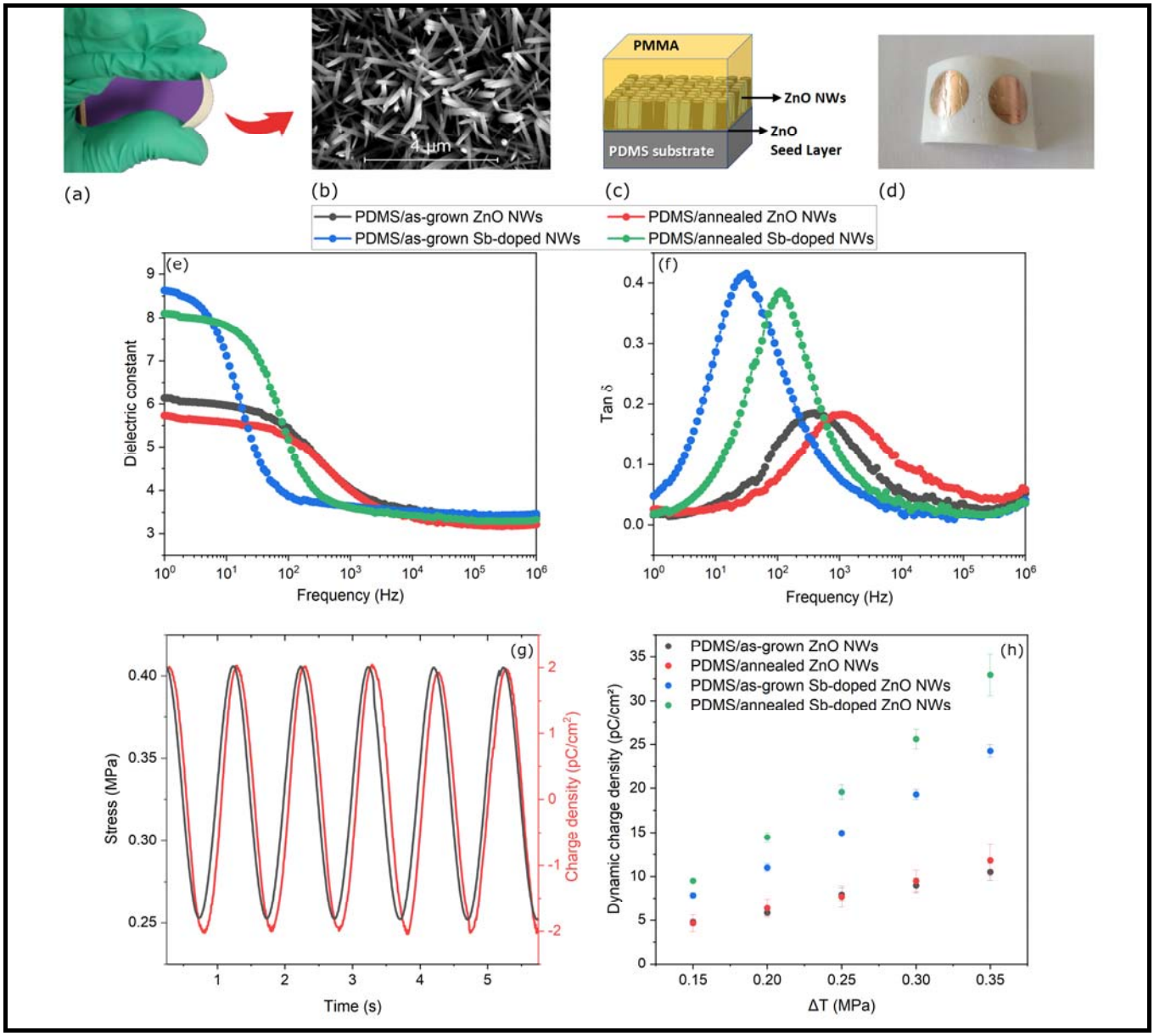

Figure 6. (a) Photograph and (b) top-view FESEM image of ZnO NWs grown on a flexible PDMS substrate by CBD with a $[SbG_2^-]$ / $[Zn(NO_3)_2]$ ratio of 1.0 % in the low-pH region. (c) Schematic of flexible PDMS/ZnO NW array composites, and (d) photograph of flexible PDMS/as-grown Sb-doped ZnO NW array composite. (e) Dielectric constant and (f) loss tangent $(\tan\delta)$ as a function of frequency for different samples. (g) Time evolution of stress and charge density of the PDMS/as-grown ZnO NW array composite at a 0.15 MPa peak-to-peak. (h) Dynamic charge density versus dynamic stress for different samples. The piezoelectric characterization was performed under a 1 Hz dynamic stress.

The dielectric constant measurements of flexible PDMS/ZnO NW array composites in the different as-grown, Sb-doped, and annealed configurations are presented in **Figure 6e,f**. Compared to the flexible PDMS/as-grown ZnO NW array composite (black curve) exhibiting a typical behavior,[64] a large difference in the dielectric constant and in the loss tangent peak of the flexible PDMS/Sb-doped ZnO NW array composites (blue and green curves)

was found. This phenomenon is supposed to arise from the significant incorporation of Sb dopants into ZnO NWs. In contrast, the thermal annealing has a smaller impact on the dielectric properties, where a similar behavior is observed between the flexible PDMS/as-grown (black curve) and PDMS/annealed (red curve) ZnO NW array composites. The loss tangent ($\tan\delta$) of all flexible ZnO NW array composites measured at low frequencies (*i.e.* below 1 Hz) was found to be smaller than 1, indicating, to some extent, a relevant dielectric behavior (without any leakage effect).[119, 120]

The piezoelectric properties of flexible PDMS/ZnO NW array composites in the different as-grown, Sb-doped, and annealed configurations are presented in **Figure 6g,h**. A periodic variation of the charge density of the PDMS/as-grown ZnO NW array composite in response to a periodic mechanical stress with 0.15 MPa magnitude and 1 Hz frequency is shown in **Figure 6g**. This confirms the linear piezoelectric effect operating in the PDMS/as-grown ZnO NW array composite, where the charge density is revealed to be in phase and expose a similar trend with respect to the applied mechanical stress. As depicted in **Figure 6h**, the specific dynamic charge density (D) was measured with respect to the increasing dynamic mechanical stress (ΔT), allowing to compute the d_{33} value for the flexible ZnO NW array composites in the different as-grown, Sb-doped, and annealed configurations. D linearly increases with ΔT, from which the d_{33} value can be estimated from the slope of the D-ΔT curves as reported in **Table 4**. It is worth noticing that the d_{33} value of the flexible PDMS/as-grown ZnO NW array composite of ~0.288 pC/N is far lower than that of the rigid Si/as-grown ZnO NW array composite of ~1.21 pC/N as developed in our previous study.[64] No matter the top layer or the bottom substrate, the polymer stacked layer acts as an insulating component to couple the piezoelectric and electrostatic effects. Therefore, according to classical electrostatics, the increased thickness of the polymer could reduce the output potential and therefore the effective d_{33} piezoelectric charge coefficient which has been proved by experimental data and COMSOL simulations.[64] Adding a flexible PDMS dielectric substrate, instead of the semiconductor Si substrate, absolutely results in a lower d_{33} piezoelectric charge coefficient. However, for the application perspective, the flexible composites, despite their lower piezoelectric sensitivity, exhibit further advantages in terms of implementation and reliability. More interestingly, the d_{33} value of the flexible PDMS/annealed ZnO NW array composite (~0.338 pC/N) is somewhat higher than that of the flexible PDMS/as-grown ZnO NW array composite, which was previously confirmed by the fact that there is no significant change in their dielectric properties. The improvement induced by the thermal annealing of as-grown ZnO NWs is related to the decrease in the concentration of H-related defects acting as shallow donors, specifically H_{BC} and V_{Zn}-

3H defect complexes as reported in ref.[35]. More importantly, the flexible PDMS/as-grown Sb-doped ZnO NW array composite achieves an almost threefold improvement (~0.763 pC/N) of the d_{33} value as compared to the flexible PDMS/as-grown ZnO NW array composite, and even an almost fourfold increase (~1.055 pC/N) when the thermal annealing has been implemented. First-principle calculations have shown that the formation energy of Sb_{Zn} is high such that their concentration is low.[49, 50] Instead, the large-size-mismatched impurity doping with Sb preferentially form Sb_{Zn}-$2V_{Zn}$[49] and Sb_i-$3V_{Zn}$[50] defect complexes with a relatively low formation energy and acting as acceptors with an ionization energy of around 0.15 and 0.28 eV, respectively. In the flexible PDMS/as-grown Sb-doped ZnO NW array composite, a significant proportion of the Sb-related defects is thus expected to be ionized and to provide free holes, recombining with the free electrons provided by the H-related defects and in turn reducing the screening of the piezoelectric potential. In the flexible PDMS/annealed Sb-doped ZnO NW array composite, the expected proportion of Sb-related defects that are ionized is even greater to more strongly reduce the screening of the piezoelectric potential. The decrease in the concentration of H-related defects acting as shallow donors is also superimposed after the thermal annealing of Sb-doped ZnO NWs. As a consequence, the d_{33} value of flexible PDMS/ZnO NW array composites is considerably enhanced by the Sb-doping and thermal annealing under oxygen atmosphere, drastically reducing the screening of the piezoelectric potential that is essentially caused by the high density of free electrons in ZnO NWs. The piezoelectric voltage coefficient (g_{33}) was then computed for the different as-grown, Sb-doped, and annealed configurations as follows:[121, 122]

$$g_{33} = \frac{d_{33}}{\varepsilon_0 \varepsilon_r} \qquad (2)$$

where ε_r is the dielectric constant and ε_0 is the vacuum permittivity ($\varepsilon_0 = 8.854\ 10^{-12} F/m$). The g_{33} piezoelectric voltage coefficient, indicating the electric field generated by a piezoelectric material per unit of mechanical stress applied, is relevant to assess the suitability of a piezoelectric material for sensing and energy harvesting applications. Also, g_{33} is a widely used parameter to compare the properties of piezoelectric materials, as it incorporates both its d_{33} piezoelectric charge coefficient and its ε_r dielectric constant. The values of g_{33} (mVm/N) at 1 Hz and 1 kHz of the flexible PDMS/ZnO NW array composites in the different as-grown, Sb-doped, and annealed configurations are reported in **Table 4**. In the application of cardiac surgery, a low-frequency sensor device working at 1–1.5 Hz is required as the heart rate of a normal adult lies in the range of 60–100 times per minute. A higher-frequency sensor device working at 1 kHz could be involved in other applications such as impact detection and vibration

measurements. The flexible PDMS/annealed Sb-doped ZnO NW array composite leads to the highest g_{33} value of 14.91 and 33.14 mVm/N at 1 Hz and 1 kHz, respectively, with respect to the other configurations. Regardless of the configuration, the g_{33} value increases as the frequency is increased from 1 Hz to 1 kHz, which is due to the decrease in the dielectric constant at higher frequency as indicated in **Figure 6e**.

Table 4. d_{33} and g_{33} values determined for flexible PDMS/ZnO NW array composites in the different as-grown, Sb-doped, and annealed configurations from experimental measurements.

Sample	d_{33} (pC/N)	g_{33} (mVm/N) at 1 Hz	g_{33} (mVm/N) at 1 kHz
PDMS/as-grown ZnO NWs	0.288 ± 0.020	5.25	8.14
PDMS/annealed ZnO NWs	0.338 ± 0.018	6.83	9.56
PDMS/as-grown Sb-doped ZnO NWs	0.763 ± 0.046	10.03	23.97
PDMS/annealed Sb-doped ZnO NWs	1.055 ± 0.035	14.91	33.14

To better assess the sensing characteristics of the developed flexible PDMS/ZnO NW array composites, a direct comparison of its d_{33} and g_{33} piezoelectric coefficients with those of other typical piezoelectric composites was carried out, as reported in **Table 5**. Two categories related to the different architectures were defined as follows. Category 1 is composed of vertically aligned annealed Sb-doped ZnO NW arrays grown by CBD on flexible PDMS and vertically aligned as-grown ZnO NW arrays grown by CBD on rigid Si substrate [64]. Category 2 consists of quasi-spherical particles of ZnO,[63] $BaTiO_3$,[123] and PZT [124] of 10 μm, 0.5 μm, and 4 μm diameter, respectively, with a 24% volume fraction incorporated into PDMS matrix using a casting method. To create a chain-like structure along the thickness direction of the composite, the particles were aligned within the polymer matrix by dielectrophoresis. In the case of Category 1, the rigid piezoelectric composites made of as-grown ZnO NWs exhibit higher d_{33} and g_{33} values than the flexible piezoelectric composites made of annealed Sb-doped ZnO NWs, but they are more fragile and their integration into medical devices is much more difficult. In the case of Category 2, the weaker intrinsic piezoelectric property of ZnO as compared to the conventional piezoelectric materials such as $BaTiO_3$ and PZT results in the fabrication of flexible piezoelectric composites made of ZnO particles with very low d_{33} and g_{33} values. A couple of important statements arise from the direct comparison of the characteristics of the different architectures between Category 1 and Category 2. First, the piezoelectric composites made of ZnO NWs have much higher d_{33} and g_{33} values than the piezoelectric composites made of ZnO particles. Second, thanks to its ultimately low dielectric constant, the piezoelectric composites made of ZnO NWs achieve a g_{33} value that is comparable to the g_{33} value of the piezoelectric composites made of other lead-free piezoelectric materials such as

$BaTiO_3$ [123] and PZT,[124] although their d_{33} values are much lower than the ones of $BaTiO_3$ and PZT. It is worth noticing here that the main advantages of ZnO over other conventional piezoelectric materials are related to the fact that no poling process is needed prior to its use and that a higher temperature stability is offered. To some extent, the poling process of almost all piezoelectric materials could be suffered from the ageing effect, which strongly depends on the environment conditions. The engineering of Sb dopants and H-related defects in ZnO NWs grown by CBD thus appears as a valuable route to improve their piezoelectric properties and thus their applicability, for instance in piezoelectric dynamic strain sensors for medical devices.

Table 5. d_{33}, g_{33} (at 1 kHz), V, Y, FoM_d, and FoM_g values for different piezoelectric composites.

	Materials	d_{33} **(pC/N)**	g_{33} **(mVm/N)**	V **(%)**	Y **(MPa)**	FoM_d **(pC N^{-1} MPa^{-1})**	FoM_g **(mV m N^{-1} MPa^{-1})**	**Ref.**
Category 1	PDMS/annealed Sb-doped ZnO NWs	1.055	33.14	0.2	2	263.8	8285.0	This Work
	Si/as-grown ZnO NWs	3.40	96.13	0.2	10000	0.2	4.8	[64]
Category 2	PDMS/ZnO	0.45	4.24	24	6	0.3	2.9	[63]
	PDMS/$BaTiO_3$	9.53	60.00	24	6	6.6	41.7	[123]
	PDMS/PZT	12.00	88.50	24	6	8.3	61.5	[124]

To assess more deeply the characteristics of the developed flexible PDMS/ZnO NW array composites, a figure-of-merit (denoted *FoM*) that not only considers the piezoelectric coefficients, but also the volume fraction (denoted V) in the different architectures, was defined. To fulfill the requirement of medical devices, the flexibility figured by the Young's modulus (denoted Y) is also a relevant parameter to be considered. The two *FoMs* of the dynamic strain sensors including FoM_d and FoM_g respectively related to d_{33} and g_{33} are thus expressed as:

$$FoM\_d = \frac{d_{33}}{Y \times V} \quad , \quad FoM\_g = \frac{g_{33}}{Y \times V} \qquad (3)$$

In the case of Category 1, the volume fraction of ZnO NWs can be approximated as the ratio between the length of ZnO NWs (~ 1 μm) and the PDMS thickness (~ 500 μm), which equals 0.2 vol%. Note that the ZnO seed layer is neglected as its thickness of around 40 nm is sufficiently small with respect to the length of ZnO NWs. The mechanical properties of piezoelectric composites can be predicted using different theoretical models. For a two-phase material as in the case of Category 1, the rule of mixture is the simplest way to predict the Young's modulus based on the arrangement of phases. The effective Young's modulus of composites (Y_{eff}) made of ZnO NWs is given by a parallel model as follows:[125]

$$Y_{eff} = Y_f V_f + Y_m V_m \quad (4)$$

where Y and V represent the Young's modulus and volume fraction, respectively. The subscripts f and m denote the two phases corresponding to the active filler and polymer matrix, respectively. As $V_f \ll V_m$, Y_{eff} for the piezoelectric composite made of ZnO NWs is close to the Young's modulus of the matrix phase. In the case of the flexible piezoelectric composite, Y_{eff} can be approximated to the Young's modulus of the PDMS ($Y_{eff} \sim Y_{PDMS} \sim 2$ MPa) principally contained in the matrix phase. The 2 µm-thick top PMMA layer is neglected with respect to the 500 µm-thick PDMS substrate. In the same way, in the case of the rigid piezoelectric composite, Y_{eff} can be approximated to the Young's modulus of the Si substrate ($Y_{eff} \sim Y_{Si} \sim 10$ GPa). In the case of Category 2, the Young's modulus (Y_{eff}) of the piezoelectric composite made of ZnO particles was measured equal to around 6 MPa.[126] The piezoelectric composites made of $BaTiO_3$ and PZT particles with the same volume fraction are expected to exhibit a similar Y_{eff} value ($i.e., Y_{eff} \sim 6$ MPa). Indeed, their Young's modulus (i.e., 25-260 GPa for PZT [127, 128] and 60- 120 GPa for $BaTiO_3$ [129]) is somehow revealed to be of the same order of magnitude as the one of ZnO (i.e., ~ 144 GPa [130, 131] and 61-125 GPa [132, 133]). Following that procedure, the *FoM* values for all piezoelectric composites are shown in **Table 5**. The annealed Sb-doped ZnO NWs integrated into the flexible piezoelectric composites exhibit the highest FoM values as compared to the other piezoelectric composites made of more conventional materials. In contrast, the as-grown ZnO NWs integrated into rigid piezoelectric composites exhibit much lower *FoM* values as poor as the ones of ZnO particles, despite its higher d_{33} and g_{33} piezoelectric coefficients. The present findings clearly demonstrate that the flexible piezoelectric composites made of ZnO NWs when combined with innovative and optimized processing conditions to reduce the screening effect could pave the way for their applications as dynamic strain sensors in medical devices.

4. Conclusions

In summary, the incorporation of Sb dopants into ZnO NWs spontaneously grown by CBD *via* the use of Sb glycolate and ammonia as chemical additives has been developed both in the low- and high-pH regions to proceed with their compensatory doping aiming at reducing the high density of free electrons in their center and hence at limiting the detrimental screening effect in piezoelectric devices. The selected $[SbG_2^-]$ / $[Zn(NO_3)_2]$ ratios were 0.0, 0.2 and 1.0 % while the pH_0 value was set to ~6.6 and ~10.8 for the low- and high-pH regions, respectively. By combining thermodynamic calculations with chemical and structural analyses, the incorporation of Sb dopants into

the wurtzite structure of ZnO NWs has been found to proceed through the adsorption process of SbG_2^- ion complex stabilized in the chemical bath on the positively charged surfaces from attractive electrostatic interactions. In the case of the low-pH region, both the nonpolar *m*-plane sidewalls of ZnO NWs and their polar *c*-plane top facet are positively charged, resulting in (i) the moderate axial growth promoting the formation of NWs with a flat hexagonal face and (ii) the significant incorporation of Sb dopants in the range of 0.16–0.45% as deduced from FESEM-EDS measurements. In contrast, in the case of the high-pH region, only the nonpolar *m*-plane sidewalls of ZnO NWs are positively charged, leading to (i) an increased radial growth promoting the formation of NWs with faceted terraces and (ii) the less significant incorporation of Sb dopants in the range of 0.11–0.21 % as inferred from FESEM-EDS measurements. Additionally, no residual Sb-based oxides, hydroxides and oxide-hydroxides phases have been detected using XRD and Raman scattering measurements. Interestingly, the spatial distribution of Sb dopants into ZnO NWs has been shown to be homogeneous by STEM-EDS mapping and no extended defects have been detected by HRTEM images. The Sb-doped ZnO NWs grown in the low-pH region with a 1.0 % $[SbG_2^-]$ / $[Zn(NO_3)_2]$ ratio show a strongly dampened NBE emission with a prominent DAP emission line when treated with the two-step thermal annealing using cathodoluminescence spectroscopy. They further show the occurrence of AMs related to Sb dopants in the range of 500–750 cm^{-1} using Raman scattering, the $AM_2(Sb)$ undergoing a shift from 690 to 715 cm^{-1} following the thermal annealing. This has revealed the combined effect of thermal annealing, reducing the concentration of hydrogen-related defects (i.e., H_{BC} and V_{Zn}-3H) acting as shallow donors, activating the V_{Zn}-N_O-H defect complexes acting as acceptor, and enhancing the compensatory doping with Sb. Eventually, the fabrication of flexible piezoelectric devices incorporating ZnO NWs grown on PDMS and encapsulated in a PMMA matrix to form a nanocomposite has been achieved using the vertically integration configurations. Importantly, the d_{33} and g_{33} piezoelectric coefficients have been found to jump from ~0.288 pC/N and 5.25 mVm/N when using unintentionally-doped ZnO NWs to ~1.055 pC/N and 14.91 mVm/N when using annealed Sb-doped ZnO NWs. Two *FoMs* have eventually been derived from the d_{33} and g_{33} piezoelectric coefficients and their values for flexible piezoelectric composites made of annealed Sb-doped ZnO NWs are compared to more conventional piezoelectric materials, showing their high potential for medical devices. The present findings report the efficient strategy consisting in reducing the detrimental screening effect in piezoelectric devices made of ZnO NWs by simultaneously introducing compensatory acceptors and engineering hydrogen-related defects, which represents an additional step forward to boost their characteristics as nanogenerators and sensors in the field of piezoelectric applications.

CRediT authorship contribution statement

José Villafuerte: Formal analysis, Investigation, Data curation, Writing – original draft, Writing – review & editing, Visualization, **Xiaoting Zhang**: Formal analysis, Investigation, Data curation, Writing – review & editing, Visualization, **Eirini Sarigiannidou**: Formal analysis, Investigation, Writing – review & editing, **Fabrice Donatini**: Investigation, Writing – review & editing, **Odette Chaix-Pluchery**: Investigation, Writing – review & editing, **Laetitia Rapenne**: Formal analysis, Investigation, Data curation, **Minh Quyen Le**: Validation, Formal analysis, Investigation, Data curation, Writing – review & editing, **Lionel Petit**: Resources, Supervision, Project administration, Funding acquisition, **Julien Pernot**: Validation, Resources, Data curation, Writing – review & editing, Supervision, **Vincent Consonni**: Conceptualization, Validation, Resources, Data curation, Writing – original draft, Writing – review & editing, Supervision, Project administration, Funding acquisition.

Declaration of competing interest

The authors declare that they have no competing financial interests or personal relationship than could have appeared to influence the work reported in this paper.

Data availability

Data will be made available upon request

Acknowledgements

The authors would like to thank Hervé Roussel, Grenoble, France, for his assistance in the XRD acquisitions. The authors further acknowledge the financial support from the French National Research Agency through the ROLLER (ANR-17-CE09-0033) and IMINEN (ANR-22-CE09-0032) projects. J.V. held a doctoral fellowship from the ROLLER project. This research has further benefited from some of the characterization equipment of the Grenoble INP-CMTC platform.

Supporting information

Supplementary data associated with this article can be found in the online version at…

References

[1] S. Rackauskas, N. Barbero, C. Barolo, G. Viscardi, ZnO Nanowire Application in Chemoresistive Sensing: A Review, Nanomaterials, 7 (2017) 381.
[2] A. Mirzaei, J.-H. Lee, S.M. Majhi, M. Weber, M. Bechelany, H.W. Kim, S.S. Kim, Resistive gas sensors based on metal-oxide nanowires, J. Appl. Phys., 126 (2019) 241102.
[3] Y. Kang, F. Yu, L. Zhang, W. Wang, L. Chen, Y. Li, Review of ZnO-based nanomaterials in gas sensors, Solid State Ion., 360 (2021) 115544.
[4] J. Liu, Y. Wang, J. Ma, Y. Peng, A. Wang, A review on bidirectional analogies between the photocatalysis and antibacterial properties of ZnO, J. Alloys Compd., 783 (2019) 898-918.
[5] V. Consonni, J. Briscoe, E. Karber, X. Li, T. Cossuet, ZnO nanowires for solar cells: a comprehensive review, Nanotechnology, 30 (2019) 362001.
[6] M. Willander, O. Nur, Q.X. Zhao, L.L. Yang, M. Lorenz, B.Q. Cao, J.Z. Perez, C. Czekalla, G. Zimmermann, M. Grundmann, A. Bakin, A. Behrends, M. Al-Suleiman, A. El-Shaer, A.C. Mofor, B. Postels, A. Waag, N. Boukos, A. Travlos, H.S. Kwack, J. Guinard, D.L. Dang, Zinc oxide nanorod based photonic devices: recent progress in growth, light emitting diodes and lasers, Nanotechnology, 20 (2009) 332001.
[7] D. Vanmaekelbergh, L.K. van Vugt, ZnO nanowire lasers, Nanoscale, 3 (2011) 2783-2800.
[8] R. Faiz, Zinc oxide light-emitting diodes: a review, Optical Engineering, 58 (2019) 010901.
[9] C.F. Pan, J.Y. Zhai, Z.L. Wang, Piezotronics and Piezo-phototronics of Third Generation Semiconductor Nanowires, Chem. Rev., 119 (2019) 9303-9359.
[10] Z.L. Wang, Towards Self-Powered Nanosystems: From Nanogenerators to Nanopiezotronics, Adv. Funct. Mater., 18 (2008) 3553-3567.
[11] J. Briscoe, S. Dunn, Piezoelectric nanogenerators - a review of nanostructured piezoelectric energy harvesters, Nano Energy, 14 (2015) 15-29.
[12] R. Yang, Y. Qin, C. Li, G. Zhu, Z.L. Wang, Converting Biomechanical Energy into Electricity by a Muscle-Movement-Driven Nanogenerator, Nano Lett., 9 (2009) 1201-1205.
[13] Y. Hu, C. Xu, Y. Zhang, L. Lin, R.L. Snyder, Z.L. Wang, A Nanogenerator for Energy Harvesting from a Rotating Tire and its Application as a Self-Powered Pressure/Speed Sensor, Adv. Mater., 23 (2011) 4068-4071.
[14] S.N. Cha, J.-S. Seo, S.M. Kim, H.J. Kim, Y.J. Park, S.-W. Kim, J.M. Kim, Sound-Driven Piezoelectric Nanowire-Based Nanogenerators, Adv. Mater., 22 (2010) 4726-4730.
[15] S. Lee, S.H. Bae, L. Lin, Y. Yang, C. Park, S.W. Kim, S.N. Cha, H. Kim, Y.J. Park, Z.L. Wang, Super-Flexible Nanogenerator for Energy Harvesting from Gentle Wind and as an Active Deformation Sensor, Adv. Funct. Mater., 23 (2013) 2445-2449.
[16] C. Falconi, Piezoelectric nanotransducers, Nano Energy, 59 (2019) 730-744.
[17] R.K. Pandey, J. Dutta, S. Brahma, B. Rao, C.-P. Liu, Review on ZnO-based piezotronics and piezoelectric nanogenerators: aspects of piezopotential and screening effect, J. Phys.: Mater., 4 (2021) 044011.
[18] R. Tao, M. Mouis, G. Ardila, Unveiling the Influence of Surface Fermi Level Pinning on the Piezoelectric Response of Semiconducting Nanowires, Adv. Electron. Mater., 4 (2018) 1700299.
[19] P. Anastas, N. Eghbali, Green Chemistry: Principles and Practice, Chem. Soc. Rev., 39 (2010) 301-312.
[20] F.R. Fan, W. Tang, Z.L. Wang, Flexible Nanogenerators for Energy Harvesting and Self-Powered Electronics, Adv. Mater., 28 (2016) 4283-4305.
[21] L. Vayssieres, Growth of arrayed nanorods and nanowires of ZnO from aqueous solutions, Adv. Mater., 15 (2003) 464-466.
[22] K.M. McPeak, M.A. Becker, N.G. Britton, H. Majidi, B.A. Bunker, J.B. Baxter, In Situ X-ray Absorption Near-Edge Structure Spectroscopy of ZnO Nanowire Growth During Chemical Bath Deposition, Chem. Mater., 22 (2010) 6162-6170.
[23] J.J. Cheng, S.M. Nicaise, K.K. Berggren, S. Gradecak, Dimensional Tailoring of Hydrothermally Grown Zinc Oxide Nanowire Arrays, Nano Lett., 16 (2016) 753-759.

[24] C. Lausecker, B. Salem, X. Baillin, V. Consonni, Modeling the Elongation of Nanowires Grown by Chemical Bath Deposition Using a Predictive Approach, J. Phys. Chem. C, 123 (2019) 29476-29483.
[25] R. Parize, J. Garnier, O. Chaix-Pluchery, C. Verrier, E. Appert, V. Consonni, Effects of Hexamethylenetetramine on the Nucleation and Radial Growth of ZnO Nanowires by Chemical Bath Deposition, J. Phys. Chem. C, 120 (2016) 5242-5250.
[26] J. Joo, B.Y. Chow, M. Prakash, E.S. Boyden, J.M. Jacobson, Face-selective electrostatic control of hydrothermal zinc oxide nanowire synthesis, Nat. Mater., 10 (2011) 596-601.
[27] D. Lincot, Solution growth of functional zinc oxide films and nanostructures, MRS Bull., 35 (2010) 778-789.
[28] V. Consonni, A.M. Lord, Polarity in ZnO nanowires: A critical issue for piezotronic and piezoelectric devices, Nano Energy, 83 (2021) 105789.
[29] C.G. Van de Walle, Hydrogen as a cause of doping in zinc oxide, Phys. Rev. Lett., 85 (2000) 1012-1015.
[30] A. Janotti, C.G. Van de Walle, Hydrogen multicentre bonds, Nat. Mater., 6 (2007) 44-47.
[31] M.G. Wardle, J.P. Goss, P.R. Briddon, Theory of Fe, Co, Ni, Cu, and their complexes with hydrogen in ZnO, Phys. Rev. B, 72 (2005) 155108.
[32] S.Z. Karazhanov, E.S. Marstein, A. Holt, Hydrogen complexes in Zn deficient ZnO, J. Appl. Phys., 105 (2009) 4.
[33] J. Villafuerte, F. Donatini, J. Kioseoglou, E. Sarigiannidou, O. Chaix-Pluchery, J. Pernot, V. Consonni, Zinc Vacancy–Hydrogen Complexes as Major Defects in ZnO Nanowires Grown by Chemical Bath Deposition, J. Phys. Chem. C, 124 (2020) 16652-16662.
[34] T. Cossuet, F. Donatini, A.M. Lord, E. Appert, J. Pernot, V. Consonni, Polarity-Dependent High Electrical Conductivity of ZnO Nanorods and Its Relation to Hydrogen, J. Phys. Chem. C, 122 (2018) 22767-22775.
[35] J. Villafuerte, O. Chaix-Pluchery, J. Kioseoglou, F. Donatini, E. Sarigiannidou, J. Pernot, V. Consonni, Engineering nitrogen- and hydrogen-related defects in ZnO nanowires using thermal annealing, Phys. Rev. Mater., 5 (2021) 056001.
[36] Y. Gao, Z.L. Wang, Equilibrium Potential of Free Charge Carriers in a Bent Piezoelectric Semiconductive Nanowire, Nano Lett., 9 (2009) 1103-1110.
[37] G. Romano, G. Mantini, A. Di Carlo, A. D'Amico, C. Falconi, Z.L. Wang, Piezoelectric potential in vertically aligned nanowires for high output nanogenerators, Nanotechnology, 22 (2011) 465401.
[38] R. Hinchet, S. Lee, G. Ardila, L. Montes, M. Mouis, Z.L. Wang, Performance Optimization of Vertical Nanowire-based Piezoelectric Nanogenerators, Adv. Funct. Mater., 24 (2014) 971-977.
[39] G. Tian, D. Xiong, Y.H. Su, T. Yang, Y.Y. Gao, C. Yan, W. Deng, L. Jin, H.T. Zhang, X.Q. Fan, C.M. Wang, W.L. Deng, W.Q. Yang, Understanding the Potential Screening Effect through the Discretely Structured ZnO Nanorods Piezo Array, Nano Lett., 20 (2020) 4270-4277.
[40] J. Villafuerte, E. Sarigiannidou, F. Donatini, J. Kioseoglou, O. Chaix-Pluchery, J. Pernot, V. Consonni, Modulating the growth of chemically deposited ZnO nanowires and the formation of nitrogen- and hydrogen-related defects using pH adjustment, Nanoscale Adv., 4 (2022) 1793-1807.
[41] A.M. Lord, V. Consonni, T. Cossuet, F. Donatini, S.P. Wilks, Schottky Contacts on Polarity-Controlled Vertical ZnO Nanorods, ACS Appl. Mater. Interfaces, 12 (2020) 13217-13228.
[42] J.G. Reynolds, C.L. Reynolds, Progress in ZnO Acceptor Doping: What Is the Best Strategy?, Adv. Condens. Matter Phys., 2014 (2014) 457058.
[43] R. Kobayashi, T. Kishi, Y. Katayanagi, T. Yano, N. Matsushita, Fabrication of nitrogen-doped ZnO nanorod arrays by hydrothermal synthesis and ambient annealing, RSC Adv., 8 (2018) 23599-23605.
[44] C. Lausecker, B. Salem, X. Baillin, O. Chaix-Pluchery, H. Roussel, S. Labau, B. Pelissier, E. Appert, V. Consonni, Chemical Bath Deposition of ZnO Nanowires Using Copper Nitrate as an Additive for Compensating Doping, Inorg. Chem., 60 (2021) 1612-1623.
[45] J. Briscoe, D.E. Gallardo, S. Dunn, In situ antimony doping of solution-grown ZnO nanorods, Chem. Commun., (2009) 1273-1275.
[46] F. Wang, J.-H. Seo, D. Bayerl, J. Shi, H. Mi, Z. Ma, D. Zhao, Y. Shuai, W. Zhou, X. Wang, An aqueous solution-based doping strategy for large-scale synthesis of Sb-doped ZnO nanowires, Nanotechnology, 22 (2011) 225602.
[47] K.C. Pradel, W. Wu, Y. Zhou, X. Wen, Y. Ding, Z.L. Wang, Piezotronic Effect in Solution-Grown p-Type ZnO Nanowires and Films, Nano Lett., 13 (2013) 2647-2653.
[48] Z. Huo, X. Wang, Y. Zhang, B. Wan, W. Wu, J. Xi, Z. Yang, G. Hu, X. Li, C. Pan, High-performance Sb-doped p-ZnO NW films for self-powered piezoelectric strain sensors, Nano Energy, 73 (2020) 104744.

[49] S. Limpijumnong, S.B. Zhang, S.-H. Wei, C.H. Park, Doping by Large-Size-Mismatched Impurities: The Microscopic Origin of Arsenic- or Antimony-Doped p-Type Zinc Oxide, Phys. Rev. Lett., 92 (2004) 155504.
[50] B. Puchala, D. Morgan, Stable interstitial dopant-vacancy complexes in ZnO, Phys. Rev. B, 85 (2012) 195207.
[51] U. Wahl, J.G. Correia, T. Mendonça, S. Decoster, Direct evidence for Sb as a Zn site impurity in ZnO, Appl. Phys. Lett., 94 (2009) 261901.
[52] D. Grinberg, M.-Q. Le, Y.J. Kwon, M.A. Fernandez, D. Audigier, F. Ganet, J.-F. Capsal, J.F. Obadia, P.-J. Cottinet, Mitral valve repair based on intraoperative objective measurement, Sci. Rep., 9 (2019) 4677.
[53] P. Sorajja, S. Vemulapalli, T. Feldman, M. Mack, R. Holmes David, A. Stebbins, S. Kar, V. Thourani, G. Ailawadi, Outcomes With Transcatheter Mitral Valve Repair in the United States, J. Am. Coll. Cardiol., 70 (2017) 2315-2327.
[54] D. Grinberg, P.-J. Cottinet, S. Thivolet, D. Audigier, J.-F. Capsal, M.-Q. Le, J.-F. Obadia, Measuring chordae tension during transapical neochordae implantation: Toward understanding objective consequences of mitral valve repair, J. Thor. Cardiov. Surg., 158 (2019) 746-755.
[55] D. Grinberg, A. Bruhat, P.-J. Cottinet, M.Q. Le, D.H. Adams, A. Costa, Mitral valve repair based on physical characterization of coaptation forces, J. Thor. Cardiov. Surg., 159 (2020) e181-e183.
[56] M.Q. Le, F. Ganet, D. Audigier, J.-F. Capsal, P.-J. Cottinet, Printing of microstructure strain sensor for structural health monitoring, Appl. Phys. A, 123 (2017) 354.
[57] J. DeGraff, R. Liang, M.Q. Le, J.-F. Capsal, F. Ganet, P.-J. Cottinet, Printable low-cost and flexible carbon nanotube buckypaper motion sensors, Mater. Des., 133 (2017) 47-53.
[58] V.-C. Nguyen, M.-Q. Le, A. Fimbel, S. Bernadet, Y. Hebrard, J.-F. Mogniotte, J.-F. Capsal, P.-J. Cottinet, Printing smart coating of piezoelectric composite for application in condition monitoring of bearings, Mater. Des., 215 (2022) 110529.
[59] Q. Liu, M.Q. Le, C. Richard, R. Liang, P.-J. Cottinet, J.-F. Capsal, Enhanced pseudo-piezoelectric dynamic force sensors based on inkjet-printed electrostrictive terpolymer, Org. Electron., 67 (2019) 259-271.
[60] S.Y. Chung, H.-J. Lee, T.I. Lee, Y.S. Kim, A wearable piezoelectric bending motion sensor for simultaneous detection of bending curvature and speed, RSC Adv., 7 (2017) 2520-2526.
[61] W. Deng, T. Yang, L. Jin, C. Yan, H. Huang, X. Chu, Z. Wang, D. Xiong, G. Tian, Y. Gao, H. Zhang, W. Yang, Cowpea-structured PVDF/ZnO nanofibers based flexible self-powered piezoelectric bending motion sensor towards remote control of gestures, Nano Energy, 55 (2019) 516-525.
[62] S. Guillemin, E. Appert, H. Roussel, B. Doisneau, R. Parize, T. Boudou, G. Bremond, V. Consonni, Controlling the Structural Properties of Single Step, Dip Coated ZnO Seed Layers for Growing Perfectly Aligned Nanowire Arrays, J. Phys. Chem. C, 119 (2015) 21694-21703.
[63] X. Zhang, M.-Q. Le, O. Zahhaf, J.-F. Capsal, P.-J. Cottinet, L. Petit, Enhancing dielectric and piezoelectric properties of micro-ZnO/PDMS composite-based dielectrophoresis, Mater. Des., 192 (2020) 108783.
[64] X. Zhang, J. Villafuerte, V. Consonni, J.-F. Capsal, P.-J. Cottinet, L. Petit, M.-Q. Le, Characterizing and Optimizing Piezoelectric Response of ZnO Nanowire/PMMA Composite-Based Sensor, Nanomaterials, 11 (2021) 1712.
[65] L.E. Greene, M. Law, D.H. Tan, M. Montano, J. Goldberger, G. Somorjai, P.D. Yang, General route to vertical ZnO nanowire arrays using textured ZnO seeds, Nano Lett., 5 (2005) 1231-1236.
[66] T. Cossuet, H. Roussel, J.M. Chauveau, O. Chaix-Pluchery, J.L. Thomassin, E. Appert, V. Consonni, Well-ordered ZnO nanowires with controllable inclination on semipolar ZnO surfaces by chemical bath deposition, Nanotechnology, 29 (2018) 11.
[67] S. Guillemin, E. Sarigiannidou, E. Appert, F. Donatini, G. Renou, G. Bremond, V. Consonni, Spontaneous shape transition of thin films into ZnO nanowires with high structural and optical quality, Nanoscale, 7 (2015) 16994-17003.
[68] S. Li, X. Zhang, L. Zhang, Sb_2O_3-Induced Tapered ZnO Nanowire Arrays: The Kinetics of Radial Growth and Morphology Control, J. Phys. Chem. C, 114 (2010) 10379-10385.
[69] A. Degen, M. Kosec, Effect of pH and impurities on the surface charge of zinc oxide in aqueous solution, J. Eur. Ceram. Soc., 20 (2000) 667-673.
[70] M. Valtiner, S. Borodin, G. Grundmeier, Stabilization and acidic dissolution mechanism of single-crystalline ZnO(0001) surfaces in electrolytes studied by in-situ AFM imaging and ex-situ LEED, Langmuir, 24 (2008) 5350-5358.
[71] C. Kunze, M. Valtiner, R. Michels, K. Huber, G. Grundmeier, Self-localization of polyacrylic acid molecules on polar ZnO(0001)-Zn surfaces, Phys. Chem. Chem. Phys., 13 (2011) 12959-12967.

[72] C. Verrier, E. Appert, O. Chaix-Pluchery, L. Rapenne, Q. Rafhay, A. Kaminski-Cachopo, V. Consonni, Tunable Morphology and Doping of ZnO Nanowires by Chemical Bath Deposition Using Aluminum Nitrate, J. Phys. Chem. C, 121 (2017) 3573-3583.
[73] C. Verrier, E. Appert, O. Chaix-Pluchery, L. Rapenne, Q. Rafhay, A. Kaminski-Cachopo, V. Consonni, Effects of the pH on the Formation and Doping Mechanisms of ZnO Nanowires Using Aluminum Nitrate and Ammonia, Inorg. Chem., 56 (2017) 13111-13122.
[74] P. Gaffuri, E. Appert, O. Chaix-Pluchery, L. Rapenne, M. Salaun, V. Consonni, The Path of Gallium from Chemical Bath into ZnO Nanowires: Mechanisms of Formation and Incorporation, Inorg. Chem., 58 (2019) 10269-10279.
[75] M.Y. Reza, M.M. Hossain, M.R. Karim, M.T.H. Tarafder, D.L. Hughes, Triethylammonium bis(2-oxido-2,2-diphenylacetato-κ^2O^1,O^2)antimonate(III), Acta Crystallographica Section E, 66 (2010) m116-m117.
[76] S. Guillemin, L. Rapenne, H. Roussel, E. Sarigiannidou, G. Bremond, V. Consonni, Formation Mechanisms of ZnO Nanowires: The Crucial Role of Crystal Orientation and Polarity, J. Phys. Chem. C, 117 (2013) 20738-20745.
[77] D. Kashchiev, G.M. van Rosmalen, Review: Nucleation in solutions revisited, Cryst. Res. Technol., 38 (2003) 555-574.
[78] B. Salopek, D. Krasic, S. Filipovic, Measurement and application of zeta-potential, Rudarsko-geolosko-naftni zbornik, 4 (1992) 147.
[79] D.H. Kim, N.G. Cho, K.S. Kim, S. Han, H.G. Kim, Structural and electrical properties of Sb-doped p-type ZnO thin films fabricated by RF magnetron sputtering, J. Electroceram., 22 (2009) 82-86.
[80] H. ullah, A. Iqbal, M. Zakria, A. Mahmood, Structural and spectroscopic analysis of wurtzite $(ZnO)_{1-x}(Sb_2O_3)_x$ composite semiconductor, Prog. Nat. Sci. Mater., 25 (2015) 131-136.
[81] A. Escobedo-Morales, U. Pal, Effect of In, Sb and Ga doping on the structure and vibrational modes of hydrothermally grown ZnO nanostructures, Curr. Appl. Phys., 11 (2011) 525-531.
[82] P. Zaumseil, High-resolution characterization of the forbidden Si 200 and Si 222 reflections, J. Appl. Crystallogr., 48 (2015) 528-532.
[83] R.B. Heller, J. McGannon, A.H. Weber, Precision Determination of the Lattice Constants of Zinc Oxide, J. Appl. Phys., 21 (1950) 1283-1284.
[84] R. Cusco, E. Alarcon-Llado, J. Ibanez, L. Artus, J. Jimenez, B.G. Wang, M.J. Callahan, Temperature dependence of raman scattering in ZnO, Phys. Rev. B, 75 (2007) 165202.
[85] C. Bundesmann, N. Ashkenov, M. Schubert, D. Spemann, T. Butz, E.M. Kaidashev, M. Lorenz, M. Grundmann, Raman scattering in ZnO thin films doped with Fe, Sb, Al, Ga, and Li, Appl. Phys. Lett., 83 (2003) 1974-1976.
[86] J. Serrano, A.H. Romero, F.J. Manjón, R. Lauck, M. Cardona, A. Rubio, Pressure dependence of the lattice dynamics of ZnO: An ab initio approach, Phys. Rev. B, 69 (2004) 094306.
[87] F.J. Manjón, B. Marí, J. Serrano, A.H. Romero, Silent Raman modes in zinc oxide and related nitrides, J. Appl. Phys., 97 (2005) 053516.
[88] Y. Huang, M. Liu, Z. Li, Y. Zeng, S. Liu, Raman spectroscopy study of ZnO-based ceramic films fabricated by novel sol–gel process, Mater. Sci. Eng. B, 97 (2003) 111-116.
[89] K.C. Pradel, J. Uzuhashi, T. Takei, T. Ohkubo, K. Hono, N. Fukata, Investigation of nanoscale voids in Sb-doped p-type ZnO nanowires, Nanotechnology, 29 (2018) 335204.
[90] Y. Yang, J. Qi, Q. Liao, Y. Zhang, L. Tang, Z. Qin, Synthesis and Characterization of Sb-Doped ZnO Nanobelts with Single-Side Zigzag Boundaries, J. Phys. Chem. C, 112 (2008) 17916-17919.
[91] S.T. Pantelides, The electronic structure of impurities and other point defects in semiconductors, Rev. Mod. Phys., 50 (1978) 797-858.
[92] H. Karzel, W. Potzel, M. Köfferlein, W. Schiessl, M. Steiner, U. Hiller, G.M. Kalvius, D.W. Mitchell, T.P. Das, P. Blaha, K. Schwarz, M.P. Pasternak, Lattice dynamics and hyperfine interactions in ZnO and ZnSe at high external pressures, Phys. Rev. B, 53 (1996) 11425-11438.
[93] T. Yamamoto, H. Katayama-Yoshida, Solution Using a Codoping Method to Unipolarity for the Fabrication of p-Type ZnO, Jpn. J. Appl. Phys., 38 (1999) L166.
[94] N.H. Nickel, K. Fleischer, Hydrogen local vibrational modes in zinc oxide, Phys. Rev. Lett., 90 (2003) 197402.
[95] A. Sugunan, H.C. Warad, M. Boman, J. Dutta, Zinc oxide nanowires in chemical bath on seeded substrates: Role of hexamine, J. Sol-Gel Sci. Technol., 39 (2006) 49-56.

[96] V. Strano, R.G. Urso, M. Scuderi, K.O. Iwu, F. Simone, E. Ciliberto, C. Spinella, S. Mirabella, Double Role of HMTA in ZnO Nanorods Grown by Chemical Bath Deposition, J. Phys. Chem. C, 118 (2014) 28189-28195.
[97] J.G. Reynolds, C.L. Reynolds, A. Mohanta, J.F. Muth, J.E. Rowe, H.O. Everitt, D.E. Aspnes, Shallow acceptor complexes in p-type ZnO, Appl. Phys. Lett., 102 (2013) 152114.
[98] J. Hu, H.Y. He, B.C. Pan, Hydrogen diffusion behavior in N doped ZnO: First-principles study, J. Appl. Phys., 103 (2008) 113706.
[99] E.V. Lavrov, J. Weber, F. Borrnert, C.G. Van de Walle, R. Helbig, Hydrogen-related defects in ZnO studied by infrared absorption spectroscopy, Phys. Rev. B, 66 (2002) 165205.
[100] E.V. Lavrov, F. Borrnert, J. Weber, Dominant hydrogen-oxygen complex in hydrothermally grown ZnO, Phys. Rev. B, 71 (2005) 035205.
[101] E.V. Lavrov, Infrared absorption spectroscopy of hydrogen-related defects in ZnO, Physica B, 340 (2003) 195-200.
[102] J.L. Lyons, J.B. Varley, D. Steiauf, A. Janotti, C.G. Van de Walle, First-principles characterization of native-defect-related optical transitions in ZnO, J. Appl. Phys., 122 (2017) 35704.
[103] F. Herklotz, A. Hupfer, K.M. Johansen, B.G. Svensson, S.G. Koch, E.V. Lavrov, Infrared absorption on a complex comprising three equivalent hydrogen atoms in ZnO, Phys. Rev. B, 92 (2015) 155203.
[104] Y.K. Frodason, K.M. Johansen, T.S. Bjorheim, B.G. Svensson, A. Alkauskas, Zn vacancy-donor impurity complexes in ZnO, Phys. Rev. B, 97 (2018) 104109.
[105] E.V. Lavrov, F. Herklotz, J. Weber, Identification of two hydrogen donors in ZnO, Phys. Rev. B, 79 (2009) 165210.
[106] B.K. Meyer, H. Alves, D.M. Hofmann, W. Kriegseis, D. Forster, F. Bertram, J. Christen, A. Hoffmann, M. Strassburg, M. Dworzak, U. Haboeck, A.V. Rodina, Bound exciton and donor-acceptor pair recombinations in ZnO, Phys. Status Solidi B, 241 (2004) 231-260.
[107] R. Heinhold, A. Neiman, J.V. Kennedy, A. Markwitz, R.J. Reeves, M.W. Allen, Hydrogen-related excitons and their excited-state transitions in ZnO, Phys. Rev. B, 95 (2017) 054120.
[108] J.F. Rommeluère, L. Svob, F. Jomard, J. Mimila-Arroyo, A. Lusson, V. Sallet, Y. Marfaing, Electrical activity of nitrogen acceptors in ZnO films grown by metalorganic vapor phase epitaxy, Appl. Phys. Lett., 83 (2003) 287-289.
[109] D. Pfisterer, J. Sann, D.M. Hofmann, M. Plana, A. Neumann, M. Lerch, B.K. Meyer, Incorporation of nitrogen acceptors in ZnO powder, Phys. Status Solidi B, 243 (2006) R1-R3.
[110] B.P. Zhang, N.T. Binh, Y. Segawa, K. Wakatsuki, N. Usami, Optical properties of ZnO rods formed by metalorganic chemical vapor deposition, Appl. Phys. Lett., 83 (2003) 1635-1637.
[111] Y.G. Wang, S.P. Lau, X.H. Zhang, H.H. Hng, H.W. Lee, S.F. Yu, B.K. Tay, Enhancement of near-band-edge photoluminescence from ZnO films by face-to-face annealing, J. Cryst. Growth, 259 (2003) 335-342.
[112] A. Teke, U. Ozgur, S. Dogan, X. Gu, H. Morkoc, B. Nemeth, J. Nause, H.O. Everitt, Excitonic fine structure and recombination dynamics in single-crystalline ZnO, Phys. Rev. B, 70 (2004) 195207.
[113] J.W. Sun, Y.M. Lu, Y.C. Liu, D.Z. Shen, Z.Z. Zhang, B. Yao, B.H. Li, J.Y. Zhang, D.X. Zhao, X.W. Fan, Nitrogen-related recombination mechanisms in p-type ZnO films grown by plasma-assisted molecular beam epitaxy, J. Appl. Phys., 102 (2007) 043522.
[114] H. Souissi, S. Jabri, A. Souissi, G. Amiri, P. Gemeiner, A. Lusson, P. Galtier, B. Dkhil, V. Sallet, M. Oueslati, A. Meftah, Activation of B1 silent Raman modes and its potential origin as source for phonon-assisted replicas in photoluminescence response in N-doped ZnO nanowires, J. Appl. Phys., 123 (2018) 025705.
[115] C. Soci, A. Zhang, B. Xiang, S.A. Dayeh, D.P.R. Aplin, J. Park, X.Y. Bao, Y.H. Lo, D. Wang, ZnO nanowire UV photodetectors with high internal gain, Nano Lett., 7 (2007) 1003-1009.
[116] Y.G. Wang, S.P. Lau, H.W. Lee, S.F. Yu, B.K. Tay, X.H. Zhang, H.H. Hng, Photoluminescence study of ZnO films prepared by thermal oxidation of Zn metallic films in air, J. Appl. Phys., 94 (2003) 354-358.
[117] A.M. Lord, T.G. Maffeis, A.S. Walton, D.M. Kepaptsoglou, Q.M. Ramasse, M.B. Ward, J. Koble, S.P. Wilks, Factors that determine and limit the resistivity of high-quality individual ZnO nanowires, Nanotechnology, 24 (2013) 435706.
[118] A.D. Bugallo, F. Donatini, C. Sartel, V. Sallet, J. Pernot, Metallic core conduction in unintentionally doped ZnO nanowire, Appl. Phys. Express, 8 (2015) 025001.
[119] F. Pedroli, A. Marrani, M.-Q. Le, C. Froidefond, P.-J. Cottinet, J.-F. Capsal, Processing optimization: A way to improve the ionic conductivity and dielectric loss of electroactive polymers, J. Polymer Sci. B, 56 (2018) 1164-1173.

[120] F. Pedroli, A. Marrani, M.-Q. Le, O. Sanseau, P.-J. Cottinet, J.-F. Capsal, Reducing leakage current and dielectric losses of electroactive polymers through electro-annealing for high-voltage actuation, RSC Adv., 9 (2019) 12823-12835.
[121] H. Khanbareh, V.Y. Topolov, C.R. Bowen, Experimental Studies on Effective Properties and Related Parameters of Piezo-Particulate Composites, in: H. Khanbareh, V.Y. Topolov, C.R. Bowen (Eds.) Piezo-Particulate Composites: Manufacturing, Properties, Applications, Springer International Publishing, Cham, 2019, pp. 55-85.
[122] D.A. van den Ende, B.F. Bory, W.A. Groen, S. van der Zwaag, Improving the d_{33} and g_{33} properties of 0-3 piezoelectric composites by dielectrophoresis, J. Appl. Phys., 107 (2010) 024107.
[123] G. D'Ambrogio, O. Zahhaf, M. Bordet, M.Q. Le, N. Della Schiava, R. Liang, P.-J. Cottinet, J.-F. Capsal, Structuring $BaTiO_3$ /PDMS Nanocomposite via Dielectrophoresis for Fractional Flow Reserve Measurement, Adv. Eng. Mater., 23 (2021) 2100341.
[124] G. D'Ambrogio, O. Zahhaf, Y. Hebrard, M.Q. Le, P.-J. Cottinet, J.-F. Capsal, Micro-Structuration of Piezoelectric Composites Using Dielectrophoresis: Toward Application in Condition Monitoring of Bearings, Adv. Eng. Mater., 23 (2021) 2000773.
[125] Z. Fan, P. Tsakiropoulos, A.P. Miodownik, Prediction of Young's modulus of particulate two phase composites, Mater. Sci. Technol., 8 (1992) 922-929.
[126] X. Zhang, M.-Q. Le, V.-C. Nguyen, J.-F. Mogniotte, J.-F. Capsal, D. Grinberg, P.-J. Cottinet, L. Petit, Characterization of micro-ZnO/PDMS composite structured via dielectrophoresis – Toward medical application, Mater. Des., 208 (2021) 109912.
[127] F. Te-Hua, J. Sheng-Rui, C. Der-San, Nanomechanical properties of lead zirconate titanate thin films by nanoindentation, J. Phys.: Condens. Matter, 15 (2003) 5253.
[128] B. Piekarski, D. DeVoe, M. Dubey, R. Kaul, J. Conrad, Surface micromachined piezoelectric resonant beam filters, Sens. Actuator A Phys., 91 (2001) 313-320.
[129] K. Maruyama, Y. Kawakami, F. Narita, Young's modulus and ferroelectric property of $BaTiO_3$ films formed by aerosol deposition in consideration of residual stress and film thickness, Jpn. J. Appl. Phys., 61 (2022) SN1011.
[130] M.Y. Soomro, I. Hussain, N. Bano, E. Broitman, O. Nur, M. Willander, Nanoscale elastic modulus of single horizontal ZnO nanorod using nanoindentation experiment, Nanoscale Res. Lett., 7 (2012) 146.
[131] J.E. Bradby, S.O. Kucheyev, J.S. Williams, C. Jagadish, M.V. Swain, P. Munroe, M.R. Phillips, Contact-induced defect propagation in ZnO, Appl. Phys. Lett., 80 (2002) 4537-4539.
[132] T.-H. Fang, W.-J. Chang, C.-M. Lin, Nanoindentation characterization of ZnO thin films, Mater. Sci. Eng. A, 452-453 (2007) 715-720.
[133] N. Yamamoto, H. Makino, T. Yamamoto, Young's Modulus and Coefficient of Linear Thermal Expansion of ZnO Conductive and Transparent Ultra-Thin Films, Adv. Mater. Sci. Eng., 2011 (2011) 136127.

Dr. Jose Villafuerte is a Research Engineer with a focus on Materials Science and Engineering. He obtained his Master's and Ph.D. from Université Grenoble Alpes and gained extensive research expertise at LMGP and Institut Néel. Villafuerte contributes to the development of zinc oxide nanowires (ZnO NWs) for piezoelectric sensors. His work centers on material synthesis, physicochemical properties, and device performance, aiming to advance smart sensing technologies for biomedical applications.

Dr. Xiaoting Zhang received her Ph.D. from INSA Lyon in 2022 under the supervision of Prof. Lionel Petit researching piezoelectric ZnO-based composites for medical applications. Her research focused on the design, simulation, fabrication and characterization of ZnO nanostructure-based composites and connected their macroscopic characteristics to industrial applications. Before her PhD, she obtained a Master degree in Photonics from Friedrich Schiller University Jena, Germany.

Dr. Eirini Sarigiannidou is the Grenoble INP-UGA Vice-President of International Affairs, and an Associate Professor at Phelma engineering school. After a bachelor's degree in physics and a master's degree in materials physics from Aristotle University of Thessaloniki (Greece), she completed her PhD at CEA Grenoble (France) on the topic "Electron microscopy and nanostructures of nitrides III". Since joining LMGP in 2006, she has acquired

knowledge on the chemical and crystalline growth of other classes of materials such as functional oxides, carbides, superconductors and MAX phases while pursuing the study of their structural properties based on transmission electron microscopy techniques.

Dr. Fabrice Donatini is a Research Engineer from Université Grenoble Alpes working in Institut Néel since 2008. He received his Ph.D. in Microelectronics from Grenoble INP (Grenoble, France) in 1996. His research focuses on the use and development of optical and electrical characterization techniques of wide bandgap semiconductors involving scanning electron microscopy related techniques for measuring down to the nanometer scale.

Dr. Odette Chaix-Pluchery is a Senior Research Scientist in CNRS. She obtained her Ph.D. in Physical Chemistry in 1986 from Université de Bourgogne (Dijon, France) and Institut Laue-Langevin (Grenoble, France). Her research activities focus on the use of spectroscopic techniques, mainly Raman spectroscopy, and X-ray diffraction, for structural studies of bulk, thin-film and nanostructured materials in the field of electronic materials, multifunctional oxide materials, and large gap semiconductor materials.

Ms. Laetitia Rapenne is a Research Engineer from CNRS working in LMGP since 2004. She received her Master degree in Materials Science from Université Louis Pasteur (Strasbourg, France) in 2000. Her activity focuses on the

structural characterization by transmission electron microscopy of different types of materials (nanowires, thin solid films, heterostructures...) for various applications in the field of renewable energies (solar cells), resistive memories and health (transparent and conducting materials, biomaterials).

Dr. Minh-Quyen Lê is an Associate Professor at INSA de Lyon. She received her Electrical Engineering and Master degrees in Acoustics from INSA de Lyon (Lyon, France) in 2008. She then received her Ph.D. in Electronics, Electrotechnics and Automatics from INSA de Lyon in 2011. After working one year as a post-doctoral fellow in LIRMM (Montpellier, France), she joined Ekium company as an Automation Engineer. Since joining LGEF in 2015, her research interests involve multiphysic coupling (electromechanics, magnetoelectrics, magnetothermics) based on electroactive materials with special emphasis on the characterization of sensors and actuators, development of 3D/4D printing additive manufacturing, and smart composite structuring under electric/magnetic field.

Prof. Lionel Petit is a Full Professor at Laboratoire de Génie Electrique et Ferroélectricité (LGEF). He received his PhD degree in acoustics from the INSA Lyon in 1996. From 1996 to 1998, he was R&D engineer at SOMFY Company. He then joined the INSA Lyon engineer school as Associate Professor and was named Full Professor in 2008. Its research activities are focused on the modelling, the design and the characterisation of electroactive multifunctional systems (EAPs, piezoelectrics) including sensors, actuators and energy harvesters. He co-published more than 100 peer-reviewed articles and he holds 10 international patents.

Prof. Julien Pernot is a Full Professor in Department of Physics and Engineering at Université Grenoble Alpes. His group at Institut Néel is engaged in fundamental and applied research on wide (SiC, GaN and ZnO) and ultra-wide band gap (diamond and AlN) semiconductors. His research focuses on advanced electrical characterization tools and microscopic methods for the study of bulk materials, thin films, micro- and nanowires for power electronics, LEDs and detectors. Pernot was awarded Institut Universitaire de France in 2012 and André Blondel medal in 2019. He is co-founder of DIAMFAB, a start-up company using some of his patents.

Dr. Vincent Consonni is a Senior Research Scientist in CNRS. He obtained his Ph.D. in Materials Science and Engineering in 2008 from Université Grenoble Alpes after research works carried out in CEA-LETI. He then spent post-doctoral stays in Paul-Drude-Institut in Berlin and in LTM in Grenoble to develop an expertize on semiconducting nanowires. He joined LMGP in Grenoble in 2011, where he leads the NanoMAT Team. His research focuses on the development of semiconducting nanowires with a special emphasis on the issues of chemical synthesis, doping, polarity, and related heterostructures for piezoelectric and optoelectronic devices.